

LEARNING CHAOS IN A LINEAR WAY

Anonymous authors

Paper under double-blind review

ABSTRACT

Learning long-term behaviors in chaotic dynamical systems, such as turbulent flows and climate modelling, is challenging due to their inherent instability and unpredictability. These systems exhibit positive Lyapunov exponents, which significantly hinder accurate long-term forecasting. As a result, understanding long-term statistical behavior is far more valuable than focusing on short-term accuracy. While autoregressive deep sequence models have been applied to capture long-term behavior, they often lead to exponentially increasing errors in learned dynamics. To address this, we shift the focus from simple prediction errors to preserving an invariant measure in dissipative chaotic systems. These systems have attractors, where trajectories settle, and the invariant measure is the probability distribution on attractors that remains unchanged under dynamics. Existing methods generate long trajectories of dissipative chaotic systems by aligning invariant measures, but it is not always possible to obtain invariant measures for arbitrary datasets. We propose the Poincaré Flow Neural Network (PFNN), a novel operator learning framework designed to capture behaviors of chaotic systems without any explicit knowledge of the invariant measure. PFNN employs an auto-encoder to map the chaotic system to a finite-dimensional feature space, effectively linearizing the chaotic evolution. It then learns the linear evolution operators to match the physical dynamics by addressing two critical properties in dissipative chaotic systems: (1) contraction, the system’s convergence toward its attractors, and (2) measure invariance, trajectories on the attractors following a probability distribution invariant to the dynamics. Our experiments on a variety of chaotic systems, including Lorenz **systems**, Kuramoto-Sivashinsky equation and Navier–Stokes equation, demonstrate that PFNN has more accurate predictions and physical statistics compared to competitive baselines including the Fourier Neural Operator and the Markov Neural Operator (code available at <https://anonymous.4open.science/r/PFNN-F461/README.md>).

1 INTRODUCTION

A View to Understand a Chaotic System. Imagine a box filled with 10^{24} identical gas molecules, each with specific positions and momenta. Physicists (Szász, 1996; Zund, 2002) posed the question:

Suppose the system starts in a certain state; will it eventually return to a state arbitrarily close to the initial one?

The question seems intractable for an enormous number ($\propto 10^{24}$) of coupled Hamiltonian equations governing the system evolution. However, Poincaré discovered that the system’s long-term behavior could be understood without explicit solutions (Poincaré, 1928). He showed that in a closed system with a finite measure, almost all initial states would eventually return close to their starting conditions (detailed proof refers to C.1). This is shown to be the case because the probability measure of the phase space is invariant under the dynamics. This led to the development of the *mean ergodic theorem* (Birkhoff, 1927; Koopman & Neumann, 1932; Neumann, 1932a; Birkhoff & Koopman, 1932), which asserts that in ergodic systems, time averages converge to space averages. Standing on the shoulders of these scientific giants, we recognize that while solving stepwise precise solutions for chaotic dynamics may be intractable, adopting a measure-theoretic view can significantly simplify the problem.

Understanding the behaviour of chaotic systems remains crucial for applications in weather forecasting, climate modelling, and fluid dynamics (Tang et al., 2020). Over the past decade, forecasting the long-term behavior of chaotic systems has posed a substantial challenge to the machine learning community (Yu et al., 2017; Mikhaeil et al., 2022; Wan et al., 2023). These dynamical systems are characterized by instabilities and sensitivity to initial conditions. A small perturbation to any given state can cause trajectories to diverge exponentially, a phenomenon attributed to positive Lyapunov exponents. Consequently, accurately predicting the long-term trajectory of such systems is non-trivial. To tackle these challenges, two primary streams have emerged in learning dynamical systems: 1) deep sequence models, which leverage sequential neural networks to learn the temporal patterns, and 2) operator learning, learning the integral-differential operators directly without knowing the differential equations.

Deep Sequence Models. Previous studies have focused on predicting short-term dynamics, mainly using deep sequence models by minimizing the mean squared error (MSE) of the next-step prediction. Commonly used models include recurrent neural networks (RNNs) (Lipton et al., 2015; Vlachas et al., 2020), long short-term memory networks (LSTMs) (Mikhaeil et al., 2022), **reservoir computing** (Pathak et al., 2018; Tanaka et al., 2019) and Transformers (Woo et al., 2024). These approaches have been applied to classic examples like the Lorenz 63 system (Lorenz, 1963) and turbulent flows (Pathak et al., 2018). However, due to the instability of trajectories, these methods often suffer from exponential error accumulation (Ribeiro et al., 2020), which hampers their ability to model chaotic systems effectively. To stabilize predictions, various strategies have been proposed, such as constraining the recurrence matrix to be orthogonal (Helfrich et al., 2018; Henaff et al., 2016), skew-symmetric (Chang et al., 2019), or ensuring globally stable fixed point solutions (Kag et al., 2020). However, these methods struggle with simulating chaotic systems since chaotic systems are usually hyperbolic and aperiodic (Hasselblatt & Katok, 2002). To address this issue, specialized models tailored to chaotic systems are necessary to accurately capture their complex patterns and behaviors. Recognizing that *dissipative chaotic systems with attractors exhibit ergodic behaviours*, new sequential models have been developed that go beyond simply minimizing MSEs. For instance, Jiang et al. (2024); Schiff et al. (2024) improve the learning of chaotic systems by incorporating transport distances to the invariant measure, which is assumed to be *known*. This ensures that the model’s predictions are aligned with the true distribution of the system. The methods proposed in these two papers (Jiang et al., 2024) generate samples directly from the neighborhood of the attractors and estimate the invariant probability distribution from these generated samples. **Schiff et al. (2024) removed the need for knowledge of the invariant measure of underlying systems, enabling direct measurement of the invariant distribution from trajectories. By incorporating the estimated invariant distribution as a regularized transport term, they train deep sequence models by enforcing long trajectories to match the estimated invariant distribution. However, a significant challenge for these methods lies in accurately estimating the invariant measure on attractors from arbitrary datasets, where this invariant distribution is usually unknown.**

Operator Learning. Another prominent approach to studying the long-term behavior of dynamical systems is through operator theory. Two classic methods in this domain are the transfer operator (Demers & Zhang, 2011) and the Koopman operator (Bevanda et al., 2021). The transfer operator captures the evolution of probability density functions in chaotic dynamical systems, making it a powerful tool for analyzing statistical mechanics (Lagro et al., 2017), chaos (Jiménez, 2023), and fractals (Ikeda et al., 2022). The Koopman operator, often considered the adjoint of the transfer operator, focuses on the evolution of feature functions. Both of these methods primarily aim to capture the long-term behaviors of chaotic dynamical systems with an invariant measure (Adams & Quas, 2023; Das et al., 2021; Valva & Giannakis, 2023). Although the dynamics on invariant sets govern long-term behavior (Mori & Kuramoto, 2013; Ornstein, 1989; Li et al., 2017), focusing solely on ergodic behaviors can significantly distort short-term predictions. **Traditionally, the Koopman operator is approximated using kernel methods (Ikeda et al., 2022; Kostic et al., 2022) or dynamic mode decomposition (DMD) (Williams et al., 2015; Takeishi et al., 2017). Recently, Koopman learning has emerged as a prominent approach for modeling the dynamics of differential equations by leveraging autoencoder architectures to approximate a finite-rank linear operator within a learned feature space (Lusch et al., 2018; Nathan Kutz et al., 2018; Brunton & Kutz, 2023). This approach has facilitated the development of various methods for capturing general dynamical behaviors, such as time series (Wang et al., 2022; Liu et al., 2024) or graph dynamics (Mukherjee et al., 2022). However, no specific Koopman learning framework has been designed to effectively capture the behaviors of dissipative chaos. Integrating deep learning techniques with operator theory has led to**

the development of various neural operators aimed at solving differential equations. For instance, Deep Operator Networks (DeepONet) (Lu et al., 2019) serve as universal approximators for initial value problems, while Fourier Neural Operators (FNO) (Li et al., 2020; Kovachki et al., 2021) learn deep Fourier features to minimize loss functions in Sobolev space, effectively solving differential equations with high-order terms. Both DeepONet and FNO aim to capture accurate solution operators for initial value problems in infinite-dimensional function space. **However, chaotic systems often require analysis beyond traditional initial value problems with unstable solutions, necessitating a specialized architecture to address.** To address this, the Markov Neural Operator (MNO) (Li et al., 2022) improves long-term predictions for dissipative chaotic systems by introducing a concept called an “absorbing ball.” This “absorbing ball” acts like a boundary that ensures the chaotic system does not go completely off course over time, guiding it back to a stable range. However, choosing the right size for this absorbing ball is tricky. If the ball is too large, it might make inaccurate predictions, as the system could stray too far from the actual behavior.

To address the aforementioned challenges, we propose the Poincaré Flow Neural Network (PFNN) **established on Koopman learning**, a novel model designed to capture both dynamics and long-term behaviors of dissipative chaotic systems without requiring *prior knowledge or assumptions* of the invariant measure from the raw data. **Unlike the previous Koopman deep learning methods for general dynamics (Li et al., 2017; Lusch et al., 2018; Nathan Kutz et al., 2018; Brunton & Kutz, 2023), our method is tailored to learn dissipative chaos by embedding intrinsic physical properties.** Specifically, dissipative chaos can be separated into two phases based on the physical properties: a) Contraction Phase: where the system converges toward attractors due to energy dissipation, which governs transient short-term dynamics; b) Measure-Invariant Phase: where the system fully explores the bounded invariant set according to the invariant distribution over time, enabling the derivation of statistical properties from time averages (ergodic behaviours). PFNN learns a linear contraction operator and a unitary operator to accurately model in an infinite-dimensional feature space the corresponding physical behaviors of the contraction phase and measure-invariant phase (as shown Figure 1), respectively. Our approach avoids relying on a known invariant measure for guiding long-term predictions. Instead, we employ simple one-step forward learning, regularized with physical constraints (contraction and unitary) on the linear operators.

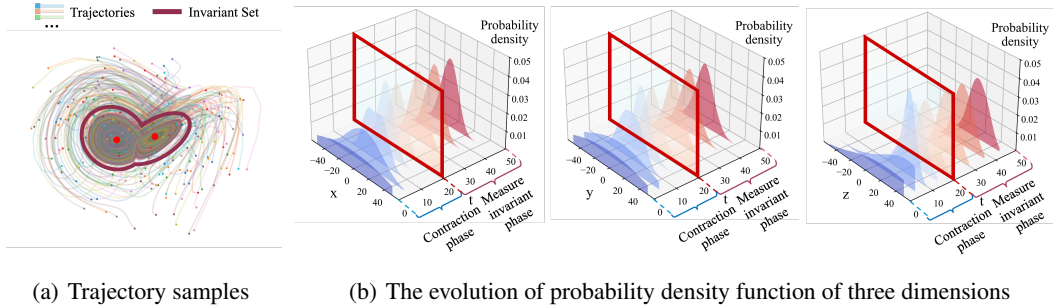


Figure 1: Contraction and measure-invariant phase in chaotic dynamics (Lorenz 63 system): (a) trajectories from random initial states all spiral toward attractors, ultimately moving within the butterfly-shaped invariant set; (b) the probability density of the trajectories samples in each state dimension keeps changing over the earlier evolution, which indicates a contraction phase in the beginning; whilst the probability density becomes invariant over the later evolution, which echos the states finally move consistently within the invariant set.

2 BACKGROUND AND PROBLEM FORMULATION

Notation. (X, \mathcal{B}, μ) denotes the measure space, with set X , Borel σ -algebra \mathcal{B} and measure μ . The forward map on the state space is denoted as T . The Lebesgue space with p -norm is represented as $\mathcal{L}^p(X, \mu)$, which is abbreviated as \mathcal{L}^p in this paper. Specifically, the Lebesgue space \mathcal{L}^2 is equipped with an inner product structure as $\langle \cdot, \cdot \rangle$. The functions ϕ, ψ are denoted as feature functions in the \mathcal{L}^2 space. \square^T denotes the transpose of a real matrix, and \square^* denotes the conjugate transpose. $\mathcal{O}(\cdot)$ denotes an asymptotically tight upper bound while $o(\cdot)$ indicate that the upper bound is not asymptotically tight. The ceiling function is denoted as $\lceil x \rceil = \min\{n \in \mathbb{Z} \mid x \leq n\}$.

Problem Setup. In what follows, we focus on forecasting dissipative chaotic dynamical systems that can be described as

$$z_{k+1} = T(z_k), z \in \mathcal{M} \subset \mathbb{R}^m, \quad (1)$$

where z_k denotes the state of the system at time $k \in \mathbb{N}$ and \mathcal{M} is a bounded space. The forward map $T : \mathcal{M} \rightarrow \mathcal{M}$ is nonlinear, pushing states from time k to time $k + 1$. The above model assumes the states depend only on the current state z_k regardless of information from long historical states.

To forecast future states, one might use a neural network to approximate the forward map T . However, the resulting model ignores prior knowledge related to the problem, and it can be challenging to analyze. In contrast, our model is based on learning the evolution of latent features $\phi \in \mathcal{L}^2$ in a linear way. This concept is fundamentally from the Koopman theory (Bevanda et al., 2021; Xiong et al., 2024; Koopman, 1931) transforming the nonlinear dynamics by a combination of nonlinear basis. In this framework, the evolution of the system becomes linear in the function space \mathcal{L}^2 . Such an evolution map is the so-called neural operator. Our model adopts the Koopman operator (Koopman, 1931), the forward map T induces a linear operator \mathcal{G} as

$$\mathcal{G}\phi = \phi \circ T, \quad (2)$$

where ϕ is the feature map as $\phi : \mathcal{M} \rightarrow \mathbb{R}$, with $\phi \in \mathcal{F} \subset \mathcal{L}^2$ being function space \mathcal{F} on \mathcal{M} . Essentially, the operator \mathcal{G} describes the linear evolution of factorized features. Consequently, future states of the features can be obtained by iteratively applying \mathcal{G} . More specifically, the feature $\phi(z_k)$ is mapped to $\phi(z_{k+1})$ under the operator \mathcal{G} . The evolution of the entire feature space can be expressed as a linear combination of features:

$$\mathcal{G}(\alpha_1\phi_1 + \alpha_2\phi_2 + \dots) = (\alpha_1\phi_1 + \alpha_2\phi_2 + \dots) \circ T, \quad (3)$$

where $\alpha_i \in \mathbb{R}$ is the weight corresponding to the feature functions ϕ_i .

Definition 2.1 (Measure Preserving Transformation and Ergodicity (Walters, 2000)) *Let (X, \mathcal{B}, μ, T) be measure preserving transformation (MPT), meaning that for every $E \in \mathcal{B}$, the measure satisfies $\mu(T^{-1}E) = \mu(E)$. MPT is said to be ergodic if, for any invariant set E , either $\mu(E) = 0$ or $\mu(X \setminus E) = 0$. In this case, μ is referred to as an ergodic measure.*

Ergodicity $T : X \rightarrow X$ ensures that $\mu(T^{-1}E) = \mu(E) \Leftrightarrow \mu(E) = \{0, 1\}$, meaning the system almost surely follows the behavior described by the invariant measure. Simply speaking, the ergodicity implies that spatial statistics are the same as the temporal statistics.

Definition 2.2 (Global Attractor (Hasselblatt & Katok, 2002)) *A compact, invariant set A is called a global attractor if, for any bounded set $B \subset \mathcal{M}$ and existing a time $k^* \in \mathbb{N}$ such that $k > k^*$ such that $T^k(B)$ is contained within the neighbourhood of A .*

In this paper, we aim to forecast dissipative chaotic dynamical systems by considering invariant measures on attractors. Given an arbitrary initial state, such systems typically converge to their attractors (an interpretation of this can be found in Appendices B.1 and B.2). Due to the dissipative nature of the dynamics, the phase space contracts, meaning that all trajectories will eventually approach specific regions within the phase space. The contraction reflects energy dissipation from a physical standpoint. Once the system enters the neighbourhood of an attractor, it becomes ergodic, and the system’s trajectories distribute across the attractor following an invariant measure that **does not vary** over time (see 2.1). Many dynamical systems have been proven to exhibit this property, including the Lorenz 63 (Tucker, 1999), Lorenz 96 (Maiocchi et al., 2024) and Kuramoto-Sivashinsky (Temam, 2012). In other words, the trajectory of a chaotic system will span the attractor in a way that accurately reflects the statistical properties of the entire invariant set, as shown in Figure 1.

3 METHOD

In the following sections, we introduce the Poincaré Flow Neural Network (PFNN) designed for forecasting dissipative chaotic dynamical systems. PFNN consists of **two** steps: first, mapping the system into a finite-dimensional feature space using an auto-encoder (AE); second, **embedding physical properties in the finite-rank operator to capture behaviors in contraction and measure-invariant phases.**

3.1 FINITE-RANK OPERATOR APPROXIMATION

A popular approach for operator learning $\mathcal{G} : \mathcal{L}^2 \rightarrow \mathcal{L}^2$ is to construct a finite-dimensional approximation. Specifically, a convergent approximation method for prediction problems can be developed by utilizing the fact that \mathcal{G} is a bounded (and therefore continuous) linear operator, without explicitly considering its spectral properties. Given an arbitrary orthonormal basis $\{\phi_1, \phi_2, \dots\}$ of \mathcal{L}^2 , we define the operator's orthogonal projection as $\Pi_L : \mathcal{L}^2 \rightarrow \text{span}\{\phi_1, \dots, \phi_L\}$. The finite-rank operator is then given by $\mathcal{G}_L = \Pi_L \mathcal{G} \Pi_L$, where the operator \mathcal{G}_L is characterized by the matrix elements $\mathcal{G}_{ij,L} = \langle \phi_i, \mathcal{G} \phi_j \rangle$ with $1 \leq i, j \leq L$. Due to the continuity of \mathcal{G} , the sequential predictions of the operator \mathcal{G}_L converge pointwise to those of \mathcal{G} on \mathcal{L}^2 .

The finite-dimensional feature space is spanned by learned adaptive features of the neural networks used in this paper. The learned encoder and decoder are denoted as $g_{\theta_1}^{\text{en}}$ and $g_{\theta_2}^{\text{de}}$, with parameters θ_1 and θ_2 respectively. Specifically, the encoder $g_{\theta_1}^{\text{en}}$ functions as the projection operator onto the learned latent feature space, effectively embedding the state space into the function space. The decoder $g_{\theta_2}^{\text{de}}$ then maps the feature space back to the original space. In this setup, the operator \mathcal{G} and θ_1, θ_2 are learned jointly by minimizing the following loss function:

$$\arg \min_{\hat{\mathcal{G}}, \theta_1, \theta_2} \mathbb{E}_{z \sim \nu} [\|\hat{\mathcal{G}} g_{\theta_1}^{\text{en}}(z_k) - g_{\theta_1}^{\text{en}}(z_{k+1})\| + \gamma \|g_{\theta_2}^{\text{de}} \circ g_{\theta_1}^{\text{en}}(z_k) - z_k\|_2], \quad (4)$$

where $\hat{\mathcal{G}}$ is the approximated finite-rank operator, and ν is data distribution. The first term in Equation 4 represents the prediction loss, while the second term accounts for the reconstruction loss with a coefficient γ denoted as Γ_{rec} . To ensure a consistent solution in the feature space, the auto-encoder must satisfy the bijective property, meaning that encoder and decoder satisfy the constrained relationship $I_d = g_{\theta_2}^{\text{de}} \circ g_{\theta_1}^{\text{en}}$, where I_d denotes the identity matrix. For the class of finite-rank operators, we prove Theorem 3.1 regarding the PFNN. This result shows that the finite-rank operator can approximate the infinite-dimensional operator with a sufficiently small error.

Theorem 3.1 (Convergence of Finite-Rank Operator) *Let $\mathcal{M} \subset \mathbb{R}^m$ be a compact set, the solution operator $\mathcal{G} : \mathcal{L}^2 \rightarrow \mathcal{L}^2$ associated to the dynamics is locally Lipschitz. Then, for a sufficient large dimension $L \in \mathbb{N}$ and a sufficiently small number $\epsilon > 0$, there exists an approximated finite-rank operator $\hat{\mathcal{G}} : \mathcal{L}^2 \rightarrow \mathcal{L}^2$ converging pointwise such that $\sup_{z \in \mathcal{M}} \|\hat{\mathcal{G}} g_{\theta_1}^{\text{en}}(z) - \mathcal{G} \phi(z)\|_2 \leq \epsilon$.*

The theorem reflects that the finite-rank operator, derived from the infinite-dimensional operator, operates in a function space spanned by learned latent feature functions. By selecting a sufficiently large L as the dimension of the latent feature space, stepwise prediction can be achieved (see the procedure in Appendix C). While the existence of the finite-rank operator can be proven, relying solely on this approximation for time-stepping can lead to exponential error accumulation. To address this, long-term predictions can be improved by incorporating physical properties. In the following sections, we introduce two loss functions designed to enhance long-term prediction accuracy. To distinguish the different operators, those applied during the contraction phase and the measure-invariant phase are denoted as \mathcal{G}_c and \mathcal{G}_m , respectively.

3.2 STAGE I: CONTRACTION PHASE

In accordance with the definition of attractors in Section 2.2, a dissipative system induces a contraction operator (Lumer & Phillips, 1961) due to the presence of attractors. In this stage, there exists a volume contraction. It means any bounded set B containing the invariant set A will contract towards A . To characterize this contraction, we constrain the spectral properties of the operator \mathcal{G}_c , ensuring $\|\mathcal{G}_c\| \leq 1$. Specifically, we focus on $\mathcal{G}_c^T \mathcal{G}_c$ instead of \mathcal{G}_c because $\mathcal{G}_c^T \mathcal{G}_c$ is symmetric (Franklin, 2012) with real, non-negative eigenvalues, and enforce the condition:

$$\langle \mathcal{G}_c \phi, \mathcal{G}_c \phi \rangle \leq \lambda^2 \|\phi\|_2^2, \quad 0 < \lambda \leq 1. \quad (5)$$

Eigenvalues of \mathcal{G}_c with a modulus bounded by 1 reflect the contraction (refer to Lumer–Phillips theorem in Appendix D). To enforce these contraction properties in practice, we introduce a specialized loss function as

$$\arg \min_{\hat{\mathcal{G}}_c, \theta_1, \theta_2} \mathbb{E}_{z \sim \nu} [\|\hat{\mathcal{G}}_c g_{\theta_1}^{\text{en}}(z_k) - g_{\theta_1}^{\text{en}}(z_{k+1})\| + \gamma_1 \Gamma_{\text{con}} + \gamma \Gamma_{\text{rec}}], \quad (6)$$

where the contraction term is defined as $\Gamma_{con} := \text{ReLU}(\sigma(\hat{\mathcal{G}}_c^T \hat{\mathcal{G}}_c - I_d)) = \max(\sigma(\hat{\mathcal{G}}_c^T \hat{\mathcal{G}}_c - I_d), 0)$ with coefficient $\gamma_1 \in (0, 1)$. $\sigma(\cdot)$ is denoted as eigenvalues of operator, and $\text{ReLU}(\sigma(\hat{\mathcal{G}}_c^T \hat{\mathcal{G}}_c - I_d))$ ¹ constraints the negative semidefinite of $\hat{\mathcal{G}}_c^T \hat{\mathcal{G}}_c - I_d$. The Γ_{con} encourages the contraction of the state space by making the eigenvalues of $\hat{\mathcal{G}}_c^T \hat{\mathcal{G}}_c$ no larger than one, based on Equation 5. The data distribution ν is lying in the bounded set as $\mathcal{M} \setminus A$, which encourages the state space to contract towards the invariant set A from outside.

However, the invariant set of the global attractor is typically not directly observable in the raw dataset. To address this, one can utilize the dissipation property to effectively truncate the dataset, preparing it for training various operators. Dissipative chaotic systems take time to approach their invariant distribution (Žnidarič, 2015), which corresponds to the relaxation time in physics (or mixing time in ergodic theory). The relaxation time is bounded by the log-Sobolev time (Bauerschmidt & Dagallier, 2024; Mori & Shirai, 2020), which provides a stronger constraint on the convergence rate to the invariant distribution. More specifically, the relaxation time estimates the time k required for a system to approach its invariant distribution μ_* over the invariant set A , starting from an arbitrary initial state. The relaxation time can be computed using the log-Sobolev inequality, typically in the form of an exponential rate decay $\mathcal{O}(\frac{1}{c_{LSI}} \log(\frac{1}{\epsilon}))$ (Feng & Iyer, 2019), where c_{LSI} represents the log-Sobolev constant and ϵ is the tolerance. In this case, the following holds: $d(\mu_k, \mu_*) \leq \epsilon$ after $k \propto \lceil \frac{1}{c_{LSI}} \log(\frac{1}{\epsilon}) \rceil$ steps, where $d(\cdot, \cdot)$ measures the total variation distance between the two distributions. Although determining the log-Sobolev constant can be challenging, it can be inferred that the probability of lying outside A is sufficiently small, such that the timestep k is proportional to $\lceil \frac{1}{c_{LSI}} \log(\frac{\|\phi\|_2}{\epsilon}) \rceil$. **Note that ϕ is the feature function of state z . Thus, the empirical calculation of relaxation time is $\lceil \frac{1}{c_{LSI}} \log(\frac{\|z\|_2}{\epsilon}) \rceil$ and the norm of state $\|z\|_2$ can be understood as energy-like quantity in physics.** As illustrated in Figure 1, the initial distribution contracts toward the invariant distribution. Thus, it is feasible to use the trajectory data before k for the training of the contraction phase.

3.3 STAGE II: MEASURE-INVARIANT PHASE

Once the system reaches the global attractor, it explores the bounded set A based on the invariant measure, with spatial and long-term temporal statistics aligned. Von Neumann (Neumann, 1932b) established that MPT induces a unitary operator on the corresponding Hilbert space \mathcal{L}^2 . Consequently, a unitary operator \mathcal{G} can be learned to describe the system’s evolution with feature space.

Proposition 3.2 (Unitary Property) *When the map T is MPT, the operator \mathcal{G}_m is unitary on \mathcal{L}^2 . That is, for all $\phi, \psi \in \mathcal{L}^2$,*

$$\langle \mathcal{G}_m \phi, \mathcal{G}_m \psi \rangle = \langle \phi, \psi \rangle, \quad (7)$$

where $\langle \phi, \psi \rangle = \int_X \langle \phi(z), \psi(z) \rangle d\mu$ is the inner product on \mathcal{L}^2 .

Theorem 3.3 (Koopman-von Neumann (KvN) Ergodic Theorem (Neumann, 1932b)) *Let (X, \mathcal{B}, μ, T) be an MPT. If $\phi \in \mathcal{L}^2$, then $\lim_{N \rightarrow \infty} \frac{1}{N} \sum_{k=0}^{N-1} \mathcal{G}_m^k \phi = \lim_{N \rightarrow \infty} \frac{1}{N} \sum_{k=0}^{N-1} \phi \circ T^k = \bar{\phi}$ where $\bar{\phi}$ is invariant. If T is ergodic, then $\bar{\phi} = \int \phi d\mu$.*

The proof can be referred to Appendix C.3 and C.4. The KvN ergodic theorem shows that for an ergodic MPT T , the associated operator \mathcal{G} is unitary, preserving norms in \mathcal{L}^2 . This means the time averages of \mathcal{L}^2 functions converge to their space averages, ensuring the long-term predictability of chaotic systems. The theorem links chaos with operator theory, providing a framework to study the statistical behavior through \mathcal{G}_m . The spectrum of the operator \mathcal{G}_m lies on the complex unit circle $\sigma(\mathcal{G}_m) \subset \{r \in \mathbb{C} \mid |r| = 1\}$, with a positive measure on both discrete and continuous spectrum for chaotic systems (Koopman & Neumann, 1932). The presence of a continuous spectrum indicates chaotic behavior, meaning the learned operator should have its spectrum densely distributed along the unit circle. The validity of the learning results can be assessed by analyzing the spectrum of the operator, as shown in Figure 2.

¹PyTorch (2014) supports the auto-differentiation of eigenvalue function of symmetric matrix or Hermitian matrix, which improves computational stability.

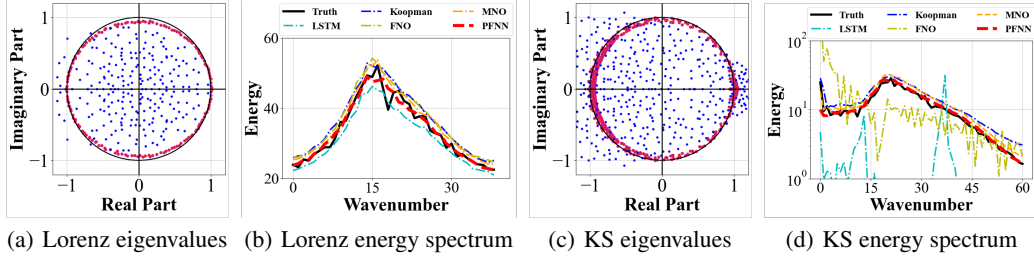


Figure 2: Operator eigenvalues and energy spectrum of the Lorenz 96 and KS equations: The **eigenvalues** in subfigures (a) and (c) display the difference of eigenvalue distribution of learnt operator layer from the aspect of the measure-invariant constraint. Red points represent the PFNN’s eigenvalues in the measure-invariant phase, densely distributed near the unit circle in the complex plane, indicating invariant measure under evolution. In contrast, blue points represent eigenvalues without the measure-invariant constraint, showing values both inside and outside the unit circle, leading to gradient vanishing and blow-up for long-term predictions. Subfigures (b) and (d) show the corresponding **energy spectrum** for the Lorenz 96 and KS equations, illustrating the system’s energy distribution across modes. The energy spectra of PFNN’s prediction fit the true energy spectra most by the introduction of the measure-invariant constraint.

To determine the unitary operator in the ergodic state (see Proposition 3.2), we leverage the intrinsic property that \mathcal{G}_m and its conjugate transpose \mathcal{G}_m^* satisfy $\mathcal{G}_m^* \mathcal{G}_m = I_d$. This property ensures that \mathcal{G}_m is unitary, preserving norms and inner products, and establishes a well-defined backward dynamic. Specifically, the backward operator \mathcal{G}_m^{-1} is equal to \mathcal{G}_m^* . This conjugate transpose relationship guarantees that $\mathcal{G}_m^* \mathcal{G}_m = \mathcal{G}_m \mathcal{G}_m^* = I_d$, indicating that \mathcal{G}_m is invertible and the inversion is consistent with unitarity (see theoretical aspects in Appendix D.3). To learn \mathcal{G}_m effectively, we use a bi-directional approach that captures both forward and backward dynamics. \mathcal{G}_m predicts the forward process, while \mathcal{G}_m^* governs the reverse. Aligning the learning of \mathcal{G}_m and \mathcal{G}_m^* ensures the operator remains unitary and accurately represents the system’s dynamics in both directions.

According to the estimated relaxation time, the trajectories of timestep $k > \lceil \frac{1}{c_{LSI}} \log(\frac{\|z\|_2}{\epsilon}) \rceil$ are used to train the measure-invariant phase. The measure-invariant loss function becomes

$$\begin{aligned} \arg \min_{\hat{\mathcal{G}}_m, \theta_1, \theta_2} \mathbb{E}_{z \sim \mu} [& \underbrace{\|\hat{\mathcal{G}}_m g_{\theta_1}^{\text{en}}(z_k) - g_{\theta_1}^{\text{en}}(z_{k+1})\|_2}_{\text{forward loss}} + \underbrace{\|\hat{\mathcal{G}}_m^* g_{\theta_1}^{\text{en}}(z_{k+1}) - g_{\theta_1}^{\text{en}}(z_k)\|_2}_{\text{backward loss}} \\ & + \gamma_2 (\underbrace{\|\hat{\mathcal{G}}_m^* \hat{\mathcal{G}}_m - I_d\|_F + \|\hat{\mathcal{G}}_m \hat{\mathcal{G}}_m^* - I_d\|_F}_{\text{consistent constraint}}) + \gamma \Gamma_{\text{rec}}], \end{aligned} \quad (8)$$

where $\gamma_2 \in (0, 1)$ is the regularized coefficient, $\|\cdot\|_F$ is denoted as the Frobenius norm, and the distribution of μ follows the distributions with timestep larger than integer k . The loss function of the first line is represented as forward and backward prediction, respectively. The last term in Equation 8 is a consistency constraint on the backward and forward process of \mathcal{G} . The combination of three terms in Equation 8 implies the unitary evolution in ergodic theorem in Sections 3.2 and 3.3.

Equations 4, 6 and 8 will be used for training the corresponding operators to predict the distinct chaotic behaviors. We provide the pseudocode in Appendix E.

4 NUMERICAL EXPERIMENTS AND ABLATION STUDY

In this section, we empirically evaluate the performance of PFNN in chaotic systems by comparing it against four baselines: (a) LSTM (Vlachas et al., 2018), a type of RNN architecture designed to learn long-term dependencies in sequential data; (b) Koopman operator (Pan et al., 2023), a linear operator that represents the evolution of functions in a dynamical system; (c) Fourier neural operator (FNO) (Kovachki et al., 2023), which uses fast Fourier transform (FFT) to efficiently parameterize integral operators and learn the system evolution; and (d) Markov neural operator (MNO) (Li et al., 2022), which enhances FNO by imposing a hard-coded constraint to better capture dissipative chaos. These baselines cover both deep sequence models and operator learning methods.

Learning tasks. (1) Lorenz 63 (Lorenz, 1963): A 3-dimensional simplified model of atmospheric convection, known for its chaotic behavior and sensitivity to initial conditions. (2) Lorenz 96 (Lorenz, 1996): A surrogate model for atmospheric circulation, characterized by the coupled differential equations with periodic boundary conditions and varying state dimensions. To test PFNN across different dimensionalities, we generated datasets with state dimensions of 9, 40, and 80, respectively. (3) Kuramoto-Sivashinsky (KS) equation (Papageorgiou & Smyrlis, 1991): A fourth-order nonlinear partial differential equation that models diffusive instabilities and chaotic behavior in systems, such as fluid dynamics, and reaction-diffusion processes. In this case, we uniformly sub-sampled 128 states from a dense spatial discretization during integration as system states. (4) Kolmogorov flow governed by Navier–Stokes (NS) equation Temam (2012): A two-dimensional shear flow commonly used in fluid dynamics to study turbulence, characterized by sinusoidal velocity fields in one direction and external forcing in the perpendicular direction. In our experiments, we utilize a 64×64 resolution field for studying.

Training details. Given the generated trajectories, each trajectory was divided into two phases: contraction and measure-invariant, with the split occurring at an estimated relaxation time. The data from each stage was then segmented into single-step pairs of observations and true states, which were subsequently shuffled to create the training data. All trajectories are sampled from random initial states, with no prior statistical information available to guide the training process.

Evaluation metrics. The models are evaluated using specific metrics: (1) Normalized Root Mean Square Error (NRMSE) for short-term performance, measuring prediction accuracy within a 10-step roll-out; (2) Kullback–Leibler divergence (KLD), and (3) Maximum Mean Discrepancy (MMD) for long-term performances, both of which compare the predicted and true distributions estimated from roll-out samples of the models and the dataset; (4) Turbulent Kinetic Energy (TKE) is distribution of turbulent energy districture, which reflects the **error of TKE between the learned model and ground truth**. Notably, KL divergence can be problematic in high-dimensional spaces, where probability distributions are overly spread out. To address this, we performed kernel principal component analysis (KPCA) to identify a low-dimensional subspace ($m = 3$), and used kernel density estimation (KDE) to estimate the predicted and true distributions. Further details on the learning tasks, training data, evaluation metrics, and baseline models can be found in Appendix G.

Table 1: Performance comparison of models (FNO, LSTM, Koopman, MNO, and PFNN) across various dynamical systems (Lorenz 63, Lorenz 96, Kuramoto-Sivashinsky, and Kolmogorov Flow) with corresponding evaluation metrics: NRMSE, KL divergence, MMD, and TKE. The best performance is highlighted in bold. **The results are evaluated 50 times using all initial states the in test set, with the uncertainties quantified as mean±standard deviation. m is the state dimension.**

	Metrics	LSTM	Koopman	FNO	MNO	PFNN
Lorenz63 ($m = 3$)	NRMSE	1.83 ± 0.85	0.67 ± 0.33	0.53 ± 0.24	0.44 ± 0.20	0.49 ± 0.26
	KLD	$+\infty$	$0.66 \pm 1.21e - 02$	$0.61 \pm 1.71e - 02$	$0.37 \pm 3.51e - 03$	$0.29 \pm 7.37e - 04$
	MMD	$1.05 \pm 3.17e - 03$	$0.46 \pm 4.37e - 06$	$0.51 \pm 2.40e - 07$	$0.48 \pm 7.60e - 07$	$0.39 \pm 4.10e - 07$
Lorenz96 ($m = 9$)	NRMSE	1.57 ± 0.44	0.61 ± 0.23	0.42 ± 0.36	0.28 ± 0.09	0.21 ± 0.14
	KLD	$3.49 \pm 1.19e - 02$	$2.61 \pm 8.29e - 03$	$2.12 \pm 5.53e - 03$	$2.01 \pm 2.47e - 03$	$1.87 \pm 2.23e - 03$
	MMD	$0.21 \pm 1.13e - 04$	$0.13 \pm 9.10e - 05$	$0.11 \pm 1.09e - 04$	$0.10 \pm 1.07e - 04$	$0.10 \pm 1.01e - 04$
Lorenz96 ($m = 40$)	NRMSE	4.77 ± 2.15	0.74 ± 0.12	0.09 ± 0.07	0.15 ± 0.04	0.11 ± 0.06
	KLD	$+\infty$	$0.16 \pm 2.32e - 04$	$0.12 \pm 1.25e - 04$	$0.11 \pm 1.78e - 04$	$0.11 \pm 1.03e - 04$
	MMD	$0.854 \pm 4.26e - 04$	$0.0239 \pm 8.62e - 06$	$0.015 \pm 2.08e - 06$	$0.011 \pm 3.11e - 06$	$0.011 \pm 1.73e - 06$
Lorenz96 ($m = 80$)	NRMSE	2.28 ± 0.73	1.64 ± 0.49	0.51 ± 0.22	0.37 ± 0.16	0.32 ± 0.09
	KLD	$1.32 \pm 5.23e - 02$	$0.24 \pm 7.96e - 03$	$0.15 \pm 2.15e - 03$	$0.18 \pm 2.73e - 03$	$0.10 \pm 1.07e - 03$
	MMD	$0.056 \pm 1.94e - 06$	$0.0088 \pm 4.00e - 08$	$0.0094 \pm 2.90e - 07$	$0.0084 \pm 4.50e - 07$	$0.0083 \pm 3.40e - 07$
KS ($m = 128$)	NRMSE	13.87 ± 4.69	1.71 ± 0.35	0.53 ± 0.29	0.31 ± 0.07	0.25 ± 0.05
	KLD	$+\infty$	52.51 ± 2.06	142.73 ± 7.63	24.53 ± 1.38	9.37 ± 0.57
	MMD	$0.996 \pm 1.11e - 03$	$0.204 \pm 3.10e - 06$	$0.915 \pm 2.91e - 03$	$0.031 \pm 8.18e - 04$	$0.011 \pm 6.31e - 06$
NS ($m = 64 \times 64$)	NRMSE	10.65 ± 4.09	10.06 ± 4.23	4.22 ± 4.23	3.81 ± 4.48	3.42 ± 3.79
	TKE	$2.29 \pm 4.07e - 02$	$1.81 \pm 3.91e - 02$	$2.10 \pm 2.55e - 02$	$1.58 \pm 2.87e - 02$	$1.36 \pm 2.20e - 02$

4.1 RESULTS AND COMPARISON

Table 1 presents the performance of all baseline methods and PFNN, evaluated using four metrics across the selected learning tasks. PFNN consistently outperforms the baselines, particularly excelling in KLD and MMD, which highlights its capability to capture the long-term dynamics of complex, chaotic systems. For short-term prediction, both PFNN and MNO show better accuracy, as reflected by the NRMSE metric. This is likely due to their ability to account for the initial phase of energy dissipation, which characterizes transient behaviors. PFNN (contraction operator) and MNO incorporate physical properties during this phase, resulting in predictions that more accurately reflect

the system’s dissipative nature. However, MNO enforces a fixed dissipation rate and pre-defined absorbing ball, which can reduce its effectiveness in short-term forecasting. Models like LSTM and Koopman, **are hard to capture transient behaviors** for states lying outside attractors, exhibit large deviations from the ground truth. Notably, while FNO uses FFT to extract features and provides relatively accurate short-term predictions, its reliance on integer Fourier modes tends to produce periodic behavior. This periodicity conflicts with the non-periodic nature of dissipative chaos.

In terms of long-term statistical properties, PFNN’s unitarity directly leads to an invariant distribution, which results in better performance in KLD and MMD. In contrast, the periodic tendencies of integer Fourier modes in FNO and MNO disrupt ergodicity, preventing a full exploration of the invariant sets. This limitation is reflected in the higher KLD and MMD values for FNO and MNO. A key observation that further validates this distinction is evident in the eigenvalue distribution of the learned unitary operator \hat{G}_m for the Lorenz 96 and KS systems. Specifically, the eigenvalues are densely distributed along the unit circle in Figure 2. This distribution aligns with the presence of a continuous spectrum in chaotic systems, as predicted by the KvN theorem, indicating a positive measure on the continuous spectrum. Additionally, Figure 2 demonstrates the effectiveness of our consistent loss function in maintaining the unitarity of the operator and accurately learning key invariant distributions, which ensures stable long-term predictions in chaotic systems. In contrast, when the model is not constrained by regularized terms in Equation 8, it results in unstable/stable modes. Empirically, this instability causes rapid forecast divergence/convergence and failure to learn the invariant distribution, as shown in the eigenvalue distributions (see blue points in Figure 2(a) and 2(c)). Furthermore, the unitarity of the operator reflects underlying conservation laws, resulting in a more accurate energy spectrum, as demonstrated in Figure 2(b), 2(d) and Figure 3. Due to the periodic behaviors in MNO and FNO, the distribution of TKE is inconsistent with ground truth. More experimental details showcasing the short- and long-term prediction and physical statistics are provided in Appendix F.

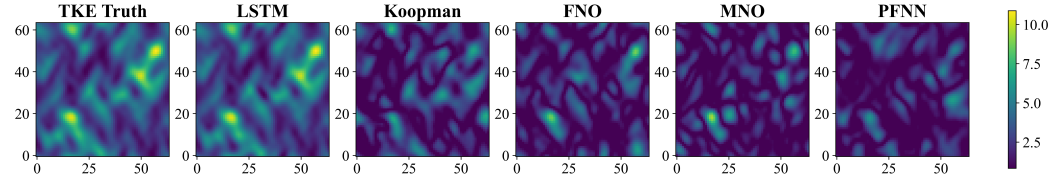


Figure 3: Visualization of the prediction error for Kolmogorov flow trajectories in terms of TKE, demonstrating the model’s accuracy in capturing the kinetic energy distribution. We compare the model-predicted trajectories with the ground truth and plot the absolute error in TKE.

4.2 ABLATION STUDY

In this section, we revisited the KS system and conducted ablation studies to evaluate the effects of key hyperparameters in PFNN, including the relaxation time k , the unitary regularized coefficient γ_2 (with γ_1 fixed²), and the finite feature dimension L . Table 2 includes the evaluated metrics for each configuration, providing insights into how these hyperparameters effect the short- and long-term performances.

Regularized coefficient. We retrained each model, systematically varying γ_2 and found that $\gamma_2 \in [0.1, 0.5]$ consistently performs well and achieves a good balance between short-term precision and long-term consistency. Outside this range, lower γ_2 reduces long-term consistency, while higher values overly constrain the model, degrading short-term accuracy.

Feature dimensions. We explored the impact of latent feature dimension L in the PFNN by varying L while keeping other hyperparameters fixed. From Table 2, we found that $L = 128, 256$ consistently perform well, while smaller values reduce the model’s expressiveness to capture complex patterns, while larger values require more data for training and risk overfitting. This ablation study result reflects a classic trade-off in deep learning between model complexity and data volume.

Log-Sobolev Constant. Systems exhibit varying dissipation rates, making it important to test different relaxation times. In most dissipative chaotic systems (Garbaczewski & Olkiewicz, 2002),

²Since the γ_1 does not affect long-term performance and is trained with a smaller dataset, we performed a grid search over $(0, 1]$ to determine its value.

the approach to the invariant distribution follows an exponential contraction rate. In this experiment, we varied the relaxation time k and constructed two corresponding datasets for training the contraction and unitary operators in PFNN. During prediction, the model first applies the contraction operator and then switches to the unitary operator after the specified relaxation time $k \propto \lceil \frac{1}{c_{LSI}} \log \frac{\|z\|_2}{\epsilon} \rceil$ (see Section 3.2). Due to the logarithmic relationship, the ϵ has a weak effect on relaxation time k . Therefore, we adjust the relaxation time by fixing $\epsilon = 0.01$ and varying the constant term $\frac{1}{c_{LSI}}$. For the KS equation, dissipation occurs primarily in the higher Fourier modes, typically for wave numbers larger than 1 (Papageorgiou & Smyrlis, 1991), and log-Sobolev constant can be bounded as $\frac{1}{c_{LSI}} \geq 1$. We test the constant as $\frac{1}{c_{LSI}} = \{1, 3, 5, 7, 9\}$, the model consistently performs well once the k exceeds a certain threshold $\frac{1}{c_{LSI}} = 5$ in KS system. Stable performance was observed when $\frac{1}{c_{LSI}} \geq 5$, highlighting that an appropriate relaxation time is crucial: if too short, it introduces bias, while if too long, many samples lie on the attractor, leading to data contamination from transient behaviors. **Furthermore, continuously increasing the parameter beyond this range does not have an obvious effect on the long-term statistics. If the hyperparameter $\frac{1}{c_{LSI}}$ is set too high, the data volume available for the measure-invariant phase in Equation 8 becomes insufficient for training.** In other experiments, we set the constant term $\frac{1}{c_{LSI}} = 5$ obtaining a similar result. A more detailed ablation study can be found in Appendix H.

Parameters Metrics	Regularized coefficient, γ_2					Feature dimension, L				Log-Sobolev Constant, $\frac{1}{c_{LSI}}$				
	0	0.1	0.3	0.5	1	64	128	256	512	1	3	5	7	9
NRMSE 100 steps	35.23	25.40	15.09	11.26	25.41	17.32	14.79	11.26	21.45	446.42	21.43	11.26	10.97	10.99
KLD	127.69	42.66	19.84	9.37	85.95	40.52	12.89	9.37	131.23	7471.44	33.66	9.37	10.94	11.28

Table 2: Ablation experiments showing the effect of varying PFNN hyperparameters. **Short-term metrics** are measuring the NRMSE with standard deviation at step 100. **Long-term metrics** are the KLD estimated with sample size 10000. Fixed hyperparameters are $\gamma_1 = 0.3$, $\gamma_2 = 0.5$, feature dimension $L = 256$ and constant term $\frac{1}{c_{LSI}}$.

5 CONCLUSIONS AND LIMITATIONS

Conclusions. Learning chaotic behavior poses a significant challenge due to the inherent instability and unpredictability of these systems. To address this complexity, we adopt a physically informed approach and introduced the Poincaré Flow Neural Network (PFNN), a novel operator learning framework designed to capture both the contraction and measure-invariant phases of dissipative chaotic systems. Our method outperforms traditional deep sequence models and neural operators, providing superior short- and long-term predictions while ensuring more consistent statistical outcomes across a variety of dissipative chaotic dynamical system experiments.

Limitations. We evaluate the limitations from both theoretical and practical perspectives. Theoretically, the assumption of ergodicity in the second stage does not apply to all chaotic systems, which can lead to a breakdown in operator unitarity for non-ergodic cases. A promising direction for future work is to extend the method to handle non-measure-preserving chaotic systems. Practically, the bi-directional training results in slow convergence due to the high computational complexity of the Frobenius norm. To alleviate this issue, future research could leverage the Hermitian properties of unitary operators or employ Hutchinson’s trace estimation to optimize trace calculations and reduce computational load. **Lastly, a promising direction is to extend the discretized-grid input in PFNN to a discretization-agnostic input.**

REFERENCES

- Terrence Adams and Anthony Quas. Ergodicity and mixing properties. In *Ergodic Theory*, pp. 35–60. Springer, 2023.
- Bipin Kumar Agarwal. *Statistical mechanics*. New Age International, 2007.
- Ayya Alieva, Dmitrii Kochkov, Jamie Alexander Smith, Michael Brenner, Qing Wang, and Stephan Hoyer. Machine learning accelerated computational fluid dynamics. *Proceedings of the National Academy of Sciences USA*, 2021.
- Roland Bauerschmidt and Benoit Dagallier. Log-sobolev inequality for near critical ising models. *Communications on Pure and Applied Mathematics*, 77(4):2568–2576, 2024.
- Petar Bevanda, Stefan Sosnowski, and Sandra Hirche. Koopman operator dynamical models: Learning, analysis and control. *Annual Reviews in Control*, 52:197–212, 2021.
- George D Birkhoff and Bernard O Koopman. Recent contributions to the ergodic theory. *Proceedings of the National Academy of Sciences*, 18(3):279–282, 1932.
- George David Birkhoff. *Dynamical systems*, volume 9. American Mathematical Soc., 1927.
- Steven L Brunton and J Nathan Kutz. Machine learning for partial differential equations. *arXiv preprint arXiv:2303.17078*, 2023.
- Bo Chang, Minmin Chen, Eldad Haber, and Ed H Chi. Antisymmetricrnn: A dynamical system view on recurrent neural networks. *arXiv preprint arXiv:1902.09689*, 2019.
- Isaac P Cornfeld, Sergei Vasilevich Fomin, and Yakov Grigor’evic Sinai. *Ergodic theory*, volume 245. Springer Science & Business Media, 2012.
- Predrag Cvitanović, Ruslan L Davidchack, and Evangelos Siminos. On the state space geometry of the kuramoto–sivashinsky flow in a periodic domain. *SIAM Journal on Applied Dynamical Systems*, 9(1):1–33, 2010.
- Suddhasattwa Das, Dimitrios Giannakis, and Joanna Slawinska. Reproducing kernel hilbert space compactification of unitary evolution groups. *Applied and Computational Harmonic Analysis*, 54: 75–136, 2021.
- Mark Demers and Hong-Kun Zhang. Spectral analysis of the transfer operator for the lorentz gas. *Journal of Modern Dynamics*, 5(4), 2011.
- Alexey Dosovitskiy, Lucas Beyer, Alexander Kolesnikov, Dirk Weissenborn, Xiaohua Zhai, Thomas Unterthiner, Mostafa Dehghani, Matthias Minderer, Georg Heigold, Sylvain Gelly, Jakob Uszkoreit, and Neil Houlsby. An image is worth 16x16 words: Transformers for image recognition at scale. *ICLR*, 2021.
- Klaus-Jochen Engel, Rainer Nagel, and Simon Brendle. *One-parameter semigroups for linear evolution equations*, volume 194. Springer, 2000.
- David P Feldman. *Chaos and dynamical systems*, volume 7. Princeton University Press, 2019.
- Yuan Yuan Feng and Gautam Iyer. Dissipation enhancement by mixing. *Nonlinearity*, 32(5):1810, 2019.
- Joel N Franklin. *Matrix theory*. Courier Corporation, 2012.
- Piotr Garbaczewski and Robert Olkiewicz. *Dynamics of dissipation*, volume 597. Springer Science & Business Media, 2002.
- Jerryman A Gyamfi. Fundamentals of quantum mechanics in liouville space. *European Journal of Physics*, 41(6):063002, 2020.
- Boris Hasselblatt and Anatole Katok. *Handbook of dynamical systems*. Elsevier, 2002.

- Kyle Helfrich, Devin Willmott, and Qiang Ye. Orthogonal recurrent neural networks with scaled cayley transform. In *International Conference on Machine Learning*, pp. 1969–1978. PMLR, 2018.
- Mikael Henaff, Arthur Szlam, and Yann LeCun. Recurrent orthogonal networks and long-memory tasks. In *International Conference on Machine Learning*, pp. 2034–2042. PMLR, 2016.
- Masahiro Ikeda, Isao Ishikawa, and Corbinian Schlosser. Koopman and perron–frobenius operators on reproducing kernel banach spaces. *Chaos: An Interdisciplinary Journal of Nonlinear Science*, 32(12), 2022.
- Ruoxi Jiang, Peter Y Lu, Elena Orlova, and Rebecca Willett. Training neural operators to preserve invariant measures of chaotic attractors. *Advances in Neural Information Processing Systems*, 36, 2024.
- Javier Jiménez. A perron–frobenius analysis of wall-bounded turbulence. *Journal of Fluid Mechanics*, 968:A10, 2023.
- Anil Kag, Ziming Zhang, and Venkatesh Saligrama. Rnns incrementally evolving on an equilibrium manifold: A panacea for vanishing and exploding gradients? In *International Conference on Learning Representations*, 2020.
- Mihail Vladimiroviĭ Karasev, Viktor Pavloviĭ Maslov, et al. *Nonlinear Poisson brackets: geometry and quantization*, volume 119. American Mathematical Soc., 2012.
- Bernard O Koopman. Hamiltonian systems and transformation in hilbert space. *Proceedings of the National Academy of Sciences*, 17(5):315–318, 1931.
- Bernard O Koopman and J v Neumann. Dynamical systems of continuous spectra. *Proceedings of the National Academy of Sciences*, 18(3):255–263, 1932.
- Vladimir Kostic, Pietro Novelli, Andreas Maurer, Carlo Ciliberto, Lorenzo Rosasco, and Massimiliano Pontil. Learning dynamical systems via koopman operator regression in reproducing kernel hilbert spaces. *Advances in Neural Information Processing Systems*, 35:4017–4031, 2022.
- Nikola Kovachki, Samuel Lanthaler, and Siddhartha Mishra. On universal approximation and error bounds for fourier neural operators. *Journal of Machine Learning Research*, 22(290):1–76, 2021.
- Nikola Kovachki, Zongyi Li, Burigede Liu, Kamyar Azizzadenesheli, Kaushik Bhattacharya, Andrew Stuart, and Anima Anandkumar. Neural operator: Learning maps between function spaces with applications to pdes. *Journal of Machine Learning Research*, 24(89):1–97, 2023.
- Matthew Lagro, Wei-Shih Yang, and Sheng Xiong. A perron–frobenius type of theorem for quantum operations. *Journal of Statistical Physics*, 169:38–62, 2017.
- Qianxiao Li, Felix Dietrich, Erik M Bollt, and Ioannis G Kevrekidis. Extended dynamic mode decomposition with dictionary learning: A data-driven adaptive spectral decomposition of the koopman operator. *Chaos: An Interdisciplinary Journal of Nonlinear Science*, 27(10), 2017.
- Zongyi Li, Nikola Kovachki, Kamyar Azizzadenesheli, Burigede Liu, Kaushik Bhattacharya, Andrew Stuart, and Anima Anandkumar. Fourier neural operator for parametric partial differential equations. *arXiv preprint arXiv:2010.08895*, 2020.
- Zongyi Li, Miguel Liu-Schiaffini, Nikola Kovachki, Burigede Liu, Kamyar Azizzadenesheli, Kaushik Bhattacharya, Andrew Stuart, and Anima Anandkumar. Learning dissipative dynamics in chaotic systems. *arXiv preprint arXiv:2106.06898*, 2022.
- Zachary C Lipton, John Berkowitz, and Charles Elkan. A critical review of recurrent neural networks for sequence learning. *arXiv preprint arXiv:1506.00019*, 2015.
- Yong Liu, Chenyu Li, Jianmin Wang, and Mingsheng Long. Koopa: Learning non-stationary time series dynamics with koopman predictors. *Advances in Neural Information Processing Systems*, 36, 2024.

- Edward N Lorenz. Deterministic nonperiodic flow. *Journal of atmospheric sciences*, 20(2):130–141, 1963.
- Edward N Lorenz. Predictability: A problem partly solved. In *Proc. Seminar on predictability*, volume 1. Reading, 1996.
- Lu Lu, Pengzhan Jin, and George Em Karniadakis. Deepnet: Learning nonlinear operators for identifying differential equations based on the universal approximation theorem of operators. *arXiv preprint arXiv:1910.03193*, 2019.
- Günter Lumer and Ralph S Phillips. Dissipative operators in a banach space. 1961.
- Bethany Lusch, J Nathan Kutz, and Steven L Brunton. Deep learning for universal linear embeddings of nonlinear dynamics. *Nature communications*, 9(1):4950, 2018.
- Chiara Cecilia Maiocchi, Valerio Lucarini, Andrey Gritsun, and Yuzuru Sato. Heterogeneity of the attractor of the lorenz’96 model: Lyapunov analysis, unstable periodic orbits, and shadowing properties. *Physica D: Nonlinear Phenomena*, 457:133970, 2024.
- Jonas Mikhaeil, Zahra Monfared, and Daniel Durstewitz. On the difficulty of learning chaotic dynamics with rnns. *Advances in Neural Information Processing Systems*, 35:11297–11312, 2022.
- Hazime Mori and Yoshiki Kuramoto. *Dissipative structures and chaos*. Springer Science & Business Media, 2013.
- Takashi Mori and Tatsuhiko Shirai. Resolving a discrepancy between liouvillian gap and relaxation time in boundary-dissipated quantum many-body systems. *Physical review letters*, 125(23):230604, 2020.
- Sayak Mukherjee, Sai Pushpak Nandanoori, Sheng Guan, Khushbu Agarwal, Subhrajit Sinha, Soumya Kundu, Seemita Pal, Yinghui Wu, Draguna L Vrabie, and Sutanay Choudhury. Learning distributed geometric koopman operator for sparse networked dynamical systems. In *Learning on Graphs Conference*, pp. 45–1. PMLR, 2022.
- J Nathan Kutz, Joshua L Proctor, and Steven L Brunton. Applied koopman theory for partial differential equations and data-driven modeling of spatio-temporal systems. *Complexity*, 2018(1): 6010634, 2018.
- J v Neumann. Physical applications of the ergodic hypothesis. *Proceedings of the National Academy of Sciences*, 18(3):263–266, 1932a.
- J v Neumann. Proof of the quasi-ergodic hypothesis. *Proceedings of the National Academy of Sciences*, 18(1):70–82, 1932b.
- Donald S Ornstein. Ergodic theory, randomness, and” chaos”. *Science*, 243(4888):182–187, 1989.
- Shaowu Pan, Eurika Kaiser, Brian M de Silva, J Nathan Kutz, and Steven L Brunton. Pykoopman: a python package for data-driven approximation of the koopman operator. *arXiv preprint arXiv:2306.12962*, 2023.
- Demetrios T Papageorgiou and Yiorgos S Smyrlis. The route to chaos for the kuramoto-sivashinsky equation. *Theoretical and Computational Fluid Dynamics*, 3(1):15–42, 1991.
- Adam Paszke, Sam Gross, Francisco Massa, Adam Lerer, James Bradbury, Gregory Chanan, Trevor Killeen, Zeming Lin, Natalia Gimelshein, Luca Antiga, Alban Desmaison, Andreas Kopf, Edward Yang, Zachary DeVito, Martin Raison, Alykhan Tejani, Sasank Chilamkurthy, Benoit Steiner, Lu Fang, Junjie Bai, and Soumith Chintala. PyTorch: An Imperative Style, High-Performance Deep Learning Library. In H. Wallach, H. Larochelle, A. Beygelzimer, F. d’Alché Buc, E. Fox, and R. Garnett (eds.), *Advances in Neural Information Processing Systems 32*, pp. 8024–8035. Curran Associates, Inc., 2019.
- Jaideep Pathak, Brian Hunt, Michelle Girvan, Zhixin Lu, and Edward Ott. Model-free prediction of large spatiotemporally chaotic systems from data: A reservoir computing approach. *Physical review letters*, 120(2):024102, 2018.

- Henri Poincaré. *Œuvres de Henri Poincaré: publiées sous les auspices de l'Académie des sciences...*, volume 1. Gauthier-Villars et cie, 1928.
- PyTorch. torch.linalg.eigh & x2014; PyTorch 2.4 documentation — pytorch.org. <https://pytorch.org/docs/stable/generated/torch.linalg.eigh.html#torch.linalg.eigh>, 2014. [Accessed 18-08-2024].
- Antônio H Ribeiro, Koen Tiels, Luis A Aguirre, and Thomas Schön. Beyond exploding and vanishing gradients: analysing rnn training using attractors and smoothness. In *International conference on artificial intelligence and statistics*, pp. 2370–2380. PMLR, 2020.
- Yair Schiff, Zhong Yi Wan, Jeffrey B Parker, Stephan Hoyer, Volodymyr Kuleshov, Fei Sha, and Leonardo Zepeda-Núñez. Dyslim: Dynamics stable learning by invariant measure for chaotic systems. *arXiv preprint arXiv:2402.04467*, 2024.
- Konrad Schmüdgen. *Unbounded self-adjoint operators on Hilbert space*, volume 265. Springer Science & Business Media, 2012.
- Domokos Szász. Boltzmann’s ergodic hypothesis, a conjecture for centuries? *Studia Scientiarum Mathematicarum Hungarica*, 31(1):299–322, 1996.
- Naoya Takeishi, Yoshinobu Kawahara, and Takehisa Yairi. Learning koopman invariant subspaces for dynamic mode decomposition. *Advances in neural information processing systems*, 30, 2017.
- Gouhei Tanaka, Toshiyuki Yamane, Jean Benoit Héroux, Ryosho Nakane, Naoki Kanazawa, Seiji Takeda, Hidetoshi Numata, Daiju Nakano, and Akira Hirose. Recent advances in physical reservoir computing: A review. *Neural Networks*, 115:100–123, 2019.
- Yang Tang, Jürgen Kurths, Wei Lin, Edward Ott, and Ljupco Kocarev. Introduction to focus issue: When machine learning meets complex systems: Networks, chaos, and nonlinear dynamics. *Chaos: An Interdisciplinary Journal of Nonlinear Science*, 30(6), 2020.
- Terence Tao. The mean ergodic theorem. <https://terrytao.wordpress.com/2008/01/30/254a-lecture-8-the-mean-ergodic-theorem/#more-250>, 2008a. [Accessed 25-08-2024].
- Terence Tao. Cohomology in dynamical system. <https://terrytao.wordpress.com/2008/12/21/cohomology-for-dynamical-systems/>, 2008b. [Accessed 13-07-2024].
- Roger Temam. *Infinite-dimensional dynamical systems in mechanics and physics*, volume 68. Springer Science & Business Media, 2012.
- Warwick Tucker. The lorenz attractor exists. *Comptes Rendus de l'Académie des Sciences-Series I-Mathematics*, 328(12):1197–1202, 1999.
- Claire Valva and Dimitrios Giannakis. Consistent spectral approximation of koopman operators using resolvent compactification. *arXiv preprint arXiv:2309.00732*, 2023.
- Pantelis R Vlachas, Wonmin Byeon, Zhong Y Wan, Themistoklis P Sapsis, and Petros Koumoutsakos. Data-driven forecasting of high-dimensional chaotic systems with long short-term memory networks. *Proceedings of the Royal Society A: Mathematical, Physical and Engineering Sciences*, 474(2213):20170844, 2018.
- Pantelis R Vlachas, Jaideep Pathak, Brian R Hunt, Themistoklis P Sapsis, Michelle Girvan, Edward Ott, and Petros Koumoutsakos. Backpropagation algorithms and reservoir computing in recurrent neural networks for the forecasting of complex spatiotemporal dynamics. *Neural Networks*, 126: 191–217, 2020.
- Felix Voigtlaender. The universal approximation theorem for complex-valued neural networks. *Applied and computational harmonic analysis*, 64:33–61, 2023.
- Peter Walters. *An introduction to ergodic theory*, volume 79. Springer Science & Business Media, 2000.

- Zhong Yi Wan, Leonardo Zepeda-Núñez, Anudhyan Boral, and Fei Sha. Evolve smoothly, fit consistently: Learning smooth latent dynamics for advection-dominated systems. *arXiv preprint arXiv:2301.10391*, 2023.
- Rui Wang, Yihe Dong, Sercan Ö Arik, and Rose Yu. Koopman neural forecaster for time series with temporal distribution shifts. *arXiv preprint arXiv:2210.03675*, 2022.
- Matthew O Williams, Ioannis G Kevrekidis, and Clarence W Rowley. A data-driven approximation of the koopman operator: Extending dynamic mode decomposition. *Journal of Nonlinear Science*, 25:1307–1346, 2015.
- Gerald Woo, Chenghao Liu, Akshat Kumar, Caiming Xiong, Silvio Savarese, and Doyen Sahoo. Unified training of universal time series forecasting transformers. *arXiv preprint arXiv:2402.02592*, 2024.
- Wei Xiong, Xiaomeng Huang, Ziyang Zhang, Ruixuan Deng, Pei Sun, and Yang Tian. Koopman neural operator as a mesh-free solver of non-linear partial differential equations. *Journal of Computational Physics*, pp. 113194, 2024.
- Rose Yu, Stephan Zheng, and Yan Liu. Learning chaotic dynamics using tensor recurrent neural networks. In *Proceedings of the ICML*, volume 17, 2017.
- Marko Žnidarič. Relaxation times of dissipative many-body quantum systems. *Physical Review E*, 92(4):042143, 2015.
- Joseph D Zund. George david birkhoff and john von neumann: A question of priority and the ergodic theorems, 1931–1932. *Historia Mathematica*, 29(2):138–156, 2002.

CONTENTS

1	Introduction	1
2	Background and Problem Formulation	3
3	Method	4
3.1	Finite-Rank Operator Approximation	5
3.2	Stage I: Contraction Phase	5
3.3	Stage II: Measure-Invariant Phase	6
4	Numerical Experiments and Ablation Study	7
4.1	Results And Comparison	8
4.2	Ablation Study	9
5	Conclusions and Limitations	10
A	Table of Notations	18
B	Dissipation and Conservation	19
C	Proofs of Main Theorems	19
C.1	Proof of Poincaré’s Claim	19
C.2	Proof of 3.1	21
C.3	Proof of 3.2	22
C.4	Proof of 3.3	22
D	Analysis on Operator	24
D.1	Theoretical Aspects of Koopman Operator	24
D.2	Contraction Operator on Hilbert Space	25
D.3	Unitary Operator	25
E	Algorithm	27
F	More Experimental Results	28
F.1	Lorenz 63	28
F.2	Lorenz 96	28
F.2.1	Experiment on 9 dimensional dataset	29
F.2.2	Experiment on 40 dimensional dataset	32
F.2.3	Experiment on 80 dimensional dataset	32
F.3	Kuramoto-Sivashinsky	37
F.4	Kolmogorov Flow	40

864	G Experiment Settings	42
865		
866	G.1 Neural Network Architecture	42
867	G.2 Dataset.	42
868	G.3 Training details and baselines.	43
869		
870	H Ablation Study	43
871		
872		
873		
874		
875		
876		
877		
878		
879		
880		
881		
882		
883		
884		
885		
886		
887		
888		
889		
890		
891		
892		
893		
894		
895		
896		
897		
898		
899		
900		
901		
902		
903		
904		
905		
906		
907		
908		
909		
910		
911		
912		
913		
914		
915		
916		
917		

A TABLE OF NOTATIONS

Notations	Meaning
c_{LSI}	log-Sobolev constant
g_{en}	encoder
g_{de}	decoder
k	time index
m	dimension of state space
z	state
A	invariant set or attractor
\mathcal{B}	Borel σ -algebra
B	bounded set
\mathcal{F}	function space
\mathcal{G}	forward operator on \mathcal{L}^2 space
\mathcal{G}_c	contraction operator
\mathcal{G}_m	unitary operator
I_d	identity matrix
$L = D \times m$	finite rank of approximated operator
\mathcal{M}	bounded state space
\mathcal{O}, o	describes limiting behavior of a function
T	nonlinear forward map
θ	parameters of neural networks
ϕ, ψ	feature functions in \mathcal{L}^2 space
μ	Lebesgue measure
μ_*	invariant distribution
$\sigma(\cdot)$	eigenvalues of operators
$d(\cdot, \cdot)$	total variation distance of probability measures
$\mathcal{L}^p(X, \mu)$	function spaces defined using a natural generalization of the p -norm
(X, \mathcal{B}, μ)	measure space

The Appendix is organized into two main sections: the first three chapters delve into theoretical analysis, while the subsequent chapters address empirical results and algorithm architectures.

We also encourage readers to spend time on the seminal monographs on ergodic theory (Birkhoff, 1927; Koopman & Neumann, 1932; Neumann, 1932a; Birkhoff & Koopman, 1932), as they offer profound insights that enrich the theoretical foundations presented in the Appendix.

B DISSIPATION AND CONSERVATION

The reason we would like to discuss Poincaré’s claim is to offer a perspective on understanding dissipative chaos from a macro-structural viewpoint. In statistical mechanics, contraction corresponds to dissipative systems, while measure preservation corresponds to conservative systems. Below, we introduce two key concepts.

Definition B.1 (Wandering Set (Hasselblatt & Katok, 2002)) *Let $T : X \rightarrow X$ be a flow map in topological space X . A point $x \in X$ is said to be a wandering point if there is a neighbourhood U of x and positive integer N such that for all $k > N$, the flow map is pairwise disjoint as*

$$T^k(U) \cap U = \emptyset. \quad (9)$$

Remark B.2 *Wandering sets are transient. When a dynamical system has a wandering set of non-zero measures, then the system is regarded as a dissipative system. This is the opposite of the conservative system in Poincaré’s claim. An intuitive way to understand the wandering set is: if a portion of phase space “wanders away” during system evolution, and never visits again, then the system is dissipative. A simple example is Lorenz 63, it will contract to the global attractor without visiting the outside again. When the global attractor exists, the invariant set can be expressed as ω -limit set as $\omega(x, T) = \bigcap_{n=1}^{\infty} \overline{\bigcup_{k=n}^{\infty} \{T^k(x)\}}$. The invariant set is thus non-wandering.*

Theorem B.3 (Liouville’s Theorem in Hamiltonian (Agarwal, 2007)) *Consider a Hamiltonian dynamical system with canonical coordinates $q_i = (q_i^1, q_i^2, q_i^3)$ and momenta $p_i = (p_i^1, p_i^2, p_i^3)$ of i -th molecule for $i = 1, \dots, N$. Then the phase space distribution $\mu(p, q)$ determines the probability $\mu(p, q)d^n q d^n p$ that the system will be found in the infinitesimal phase space volume $d^n q d^n p$. The Liouville equation governs the evolution of $\mu(p, q; t)$ in time t as*

$$\frac{d\mu}{dt} = \frac{\partial \mu}{\partial t} + \sum_{i=1}^N \left(\frac{\partial \mu}{\partial q_i} \dot{q}_i + \frac{\partial \mu}{\partial p_i} \dot{p}_i \right) = 0. \quad (10)$$

Or we can say the distribution function is constant along any trajectory in phase space.

Remark B.4 *In Hamiltonian mechanics, the phase space is a smooth manifold that comes naturally equipped with a smooth measure (locally, this measure is the $6N$ -dimensional Lebesgue measure). The theorem says this smooth measure is invariant under the Hamiltonian flow due to the preservation properties of the symplectic form. By the language in ergodic theory, we can assert that the $T : X \rightarrow X$ is a continuous conservative flow such that $\mu(E) = \mu(T^k E)$ for any $E \subset X$ and $k \in \mathbb{N}$.*

C PROOFS OF MAIN THEOREMS

C.1 PROOF OF POINCARÉ’S CLAIM

Theorem C.1 (Poincaré’s Claim) *Imagine a box filled with gas made of N identical molecules. Classical mechanics says that if we know the positions $q_i = (q_i^1, q_i^2, q_i^3)$ and momenta $p_i = (p_i^1, p_i^2, p_i^3)$ of i -th molecule for $i = 1, \dots, N$, the positions and momenta of each particles at time t determines by the Hamiltonian’s equations as*

$$\begin{aligned} \dot{p}_i^j(t) &= -\frac{\partial H}{\partial q_i^j}, \\ \dot{q}_i^j(t) &= \frac{\partial H}{\partial p_i^j}, \end{aligned} \quad (11)$$

where $H(q_1, \dots, q_N, p_1, \dots, p_N)$ is the Hamiltonian, measuring the total energy of the system.

The state of entire system is denoted as $(q, p) = (q_1, \dots, q_N, p_1, \dots, p_N)$. Let X denote the collection of all possible states. If the Hamiltonian is bounded above, then the transformation of state can be defined by a map as

$$T_t : (q, p) \rightarrow (q(t), p(t)), \quad (12)$$

where T_t push the state move towards after t steps. When the system is regular, there exist $6N$ equations as shown in Equation 11 coupled together. The problem can be regarded as an initial value problem, and T satisfies the conservative law for the Hamiltonian system, which means $x(0) \in X \Rightarrow T_t(x(0)) \in X$ for all t .

When the system with enormous molecules, Poincaré claimed that the system starts at a certain state $(q(0), p(0))$, it will eventually return to a state close to $(q(0), p(0))$ after a long enough time.

Proof. Here is Poincaré's solution. Define $T := T_1$ and $T^k = T_k$. Fix $\epsilon > 0$ and consider the set of W of all states $x = (q, p)$ such that $d(x, T^k(x)) > \epsilon$ for all $k > 1$, where $d(\cdot, \cdot)$ is the Euclidean distance. Divide W into finitely many disjoint pieces as W_i of diameter less than ϵ .

For each fixed i , the sets $T^{-k}(W_i) (k \geq 1)$ are pairwise disjoint, otherwise we can derive that $T^{-n}(W_i) \cap T^{-n-k}(W_i) \neq \emptyset \Rightarrow W_i \cap T^{-k}(W_i) \neq \emptyset$. In such a situation, this leads to a contradiction

- $x \in T^{-k}(W_i)$ implies that $T^k(x) \in W_i$, whence $d(x, T^k(x)) \leq \text{diam}(W_i) < \epsilon$,
- $x \in W_i \subset W$ implies that $d(x, T^k(x)) > \epsilon$ by the initial settings of W .

So $T^{-k}(W_i)$ must be pairwise disjoint.

Since $\{T^{-k}W_i\}_{k \geq 1}$ are pairwise disjoint, $\mu(X) \geq \sum_{k \geq 1} \mu(T^{-k}W_i)$. However, by the Liouville's theorem in statistical mechanics in B.3 Agarwal (2007)³, all $T^{-k}(W_i)$ have the same measure, and $\mu(X) < \infty$, so a natural result must be $\mu(W_i) = 0$ for all W_i . The summation of all $\mu(\bigcup_{i \in \mathbb{N}} W_i) = 0$ means the measure zero of *wandering set* (Feldman, 2019). In summary, we can infer $\mu(X \setminus \bigcup_{i \in \mathbb{N}} W_i) = 1$, and the system will explore sufficiently for all possible set $X \setminus \bigcup_{i \in \mathbb{N}} W_i$. Consequently, we have the property as $d(T^k(x), x) < \epsilon$ for $k \geq 1$.

Proposition C.2 Suppose (X, \mathcal{B}, μ, T) is an MPT on a complete measure space, then the following are equivalent (Cornfeld et al., 2012):

- μ is ergodic;
- if $E \in \mathcal{B}$ and $\mu(T^{-1}E \Delta E) = 0$ ⁴, then $\mu(E) = 0$ or $\mu(X \setminus E) = 0$;
- $f : X \rightarrow \mathbb{R}$ is a measurable function and $f \circ T = f$ almost everywhere, then there is a constant $c \in \mathbb{R}$, s.t. $f = c$ almost everywhere.

Proposition C.3 Mixing property implies ergodicity.

Proof. Suppose E is invariant, then the mixing property and measure preserving property imply $\mu(E) = \lim_{k \rightarrow \infty} \mu(E \cap T^{-k}E) \rightarrow \mu(E)^2$, whence $\mu(E)^2 = \mu(E)$. It follows that $\mu(E) = 0$ or $\mu(E) = 1 = \mu(X)$. This result reflects the second item in C.2, and thus ergodicity.

Proposition C.4 A MPT (X, \mathcal{B}, μ, T) is strongly mixing iff for every $\phi, \psi \in L^2$, $\lim_{k \rightarrow \infty} \int \phi \psi \circ T^k d\mu \rightarrow \int \phi d\mu \int \psi d\mu$, or equivalent to say $\lim_{k \rightarrow \infty} \text{Cov}(\phi, \psi \circ T^k) \rightarrow 0$.

Proof. The following fact can be easily derived as

- Fact 1. Since $\mu \circ T^{-1} = \mu$, $\|\phi \circ T\|_2 = \|\phi\|_2$, for all $\phi \in \mathcal{L}^2$;
- Fact 2. $|\text{Cov}(\phi, \psi)| \leq 4\|\phi - \int \phi\|_2 \|\psi - \int \psi\|_2$;

³The Liouville equation governs the evolution of probability space is invariant under the flow map as $\mu(T_t E) = \mu(E)$ for $E \subset X$.

⁴ Δ is the symmetric set difference such that $A \Delta B = (A \setminus B) \cup (B \setminus A)$.

- Fact 3. The function $Cov(\phi, \psi)$ is bilinear.

The proof of proposition needs to indicate it as a necessary and sufficient condition.

(Necessary.) The condition that for $\phi, \psi \in \mathcal{L}^2$, the mixing result reflects that ϕ, ψ can be regarded as the indicator function as $\phi = 1_E$ and $\psi = 1_F$. By the property, we have $\lim_{k \rightarrow \infty} Cov(\phi, \psi \circ T^k) \rightarrow 0$ according to the mixing property. Consequently, the necessity is proved.

(Sufficient.) Let ϕ, ψ be the linear combination of indicator functions on the invariant set. Generally $\phi, \psi \in \mathcal{L}^2$, giving a small perturbation $\epsilon > 0$, the finite linear combinations of indicators become $\phi_\epsilon, \psi_\epsilon$, satisfying $\|\phi - \phi_\epsilon\|_2, \|\psi - \psi_\epsilon\|_2 < \epsilon$. Then, by the analysis tricks as

$$\begin{aligned} & \lim_{k \rightarrow \infty} |Cov(\phi, \psi \circ T^k)| \\ & \leq \lim_{k \rightarrow \infty} |Cov(\phi - \phi_\epsilon, \psi_\epsilon \circ T^k)| + \lim_{k \rightarrow \infty} |Cov(\phi_\epsilon, \psi_\epsilon \circ T^k)| + \lim_{k \rightarrow \infty} |Cov(\phi_\epsilon, (\psi_\epsilon - \psi) \circ T^k)| \\ & \leq 4\epsilon\|\psi\|_2 + o(1) + 4(\|\phi\|_2 + \epsilon)\epsilon, \end{aligned} \quad (13)$$

where the result tells us $\lim_{k \rightarrow \infty} Cov(\phi, \psi \circ T^k) \leq 4\epsilon\|\psi\|_2 + o(1) + 4(\|\phi\|_2 + \epsilon)\epsilon$ according to the Fact 1, 2 and 3. When ϵ is sufficiently small, the limit becomes zero, the proof is finished.

C.2 PROOF OF 3.1

Since $\{\phi_1, \phi_2, \dots\}$ is an orthonormal basis of \mathcal{L}^2 , for L is large enough, we have a projection map as $g_{en} := \Pi_L \phi$ approximates ϕ within ϵ -bound as

$$\|\phi_L - \phi\|_2 \leq \epsilon. \quad (14)$$

Since the forward operator \mathcal{G} is locally Lipschitz bounded by a constant c , the following the inequality holds

$$\sup_{z \in \mathcal{M}} \|\mathcal{G}\phi_L - \mathcal{G}\phi\|_2 < \sup_{z \in \mathcal{M}} c\|\phi_L(z) - \phi(z)\| < c\epsilon. \quad (15)$$

Now, ϕ_L is a function lying the space of \mathcal{L}^2 since it is a linear combination of $\{\phi_i\}_{i \in I}$. The encoder map $g_{\theta_1}^{en}$ learns the adaptive feature from the dataset. When the dataset is sufficiently large, there exists a map as

$$g_{\theta_1}^{en} = \phi_L, \quad (16)$$

where g_{en} spans a finite-dimensional linear space, the relation holds due to the universal property of neural networks (Voigtlaender, 2023). In such case the learned operator $\hat{\mathcal{G}}$ can be written as

$$\hat{\mathcal{G}} = \Pi_L \mathcal{G} \Pi_L, \quad (17)$$

where the finite representation of the operator $\hat{\mathcal{G}}$ is consistent with $\mathcal{G}_L = \Pi_L \mathcal{G} \Pi_L$. Consequently, we have the inequality as

$$\begin{aligned} & \sup_{z \in \mathcal{M}} \|\hat{\mathcal{G}} \circ g_{\theta_1}^{en}(z) - \mathcal{G} \circ \phi(z)\|_2 \\ & \leq \underbrace{\sup_{z \in \mathcal{M}} \|\hat{\mathcal{G}} \circ g_{\theta_1}^{en}(z) - \hat{\mathcal{G}} \circ \phi(z)\|_2}_{\text{strongly continuous property}} + \underbrace{\sup_{z \in \mathcal{M}} \|\hat{\mathcal{G}} \circ \phi(z) - \mathcal{G} \circ \phi(z)\|_2}_{\text{condition of strong operator topology}} \\ & \leq (c + 1)\epsilon. \end{aligned} \quad (18)$$

The second line is from the triangle inequality. The third line holds due to the strongly continuous operator⁵ and strong operator topology⁶ in Hilbert space (see D.1), then uniform limit of some sequence of finite-rank operators exists. Therefore, we can assert that existing a finite rank $L \in \mathbb{N}$ to approximate the operator \mathcal{G} with arbitrary small error.

⁵1. Suppose $\{x_n\}$ a sequence of elements in \mathcal{L}^2 that converges to x in the norm of the space, i.e., $\lim_{n \rightarrow \infty} \|x_n - x\| \rightarrow 0$. The strong continuity of \mathcal{G} implies that the operator \mathcal{G} is continuous with respect to the norm topology when applied to sequences of vectors. Therefore, it must hold that $\lim_{n \rightarrow \infty} \|\mathcal{G}x_n - \mathcal{G}x\| \rightarrow 0$.

⁶Let $\mathfrak{L}(X)$ be the space of all bounded, linear operators on Hilbert space X . A net $\{\mathcal{G}_n\} \subset \mathfrak{L}(X)$ converges pointwise to $\mathcal{G} \in \mathfrak{L}(X)$ on $(X, \|\cdot\|)$ (i.e., $\lim_{n \rightarrow \infty} \|\mathcal{G}_n x - \mathcal{G}x\| \rightarrow 0, \forall x \in X$) if and only if $\{\mathcal{G}_n\}$ converges to \mathcal{G} in the strong operator topology on $\mathfrak{L}(X)$.

C.3 PROOF OF 3.2

(Unitary property.) The unitary of \mathcal{G} follows from the measure-preserving property of T . For $\phi, \psi \in \mathcal{L}^2$, we have

$$\begin{aligned} & \langle \mathcal{G}\phi, \mathcal{G}\psi \rangle \\ &= \int_X (\mathcal{G} \circ \phi(x)) \overline{(\mathcal{G} \circ \psi(x))} d\mu \\ &= \int_X (\phi(Tx)) \overline{(\psi(Tx))} d\mu(x) \end{aligned} \quad (19)$$

Using the change of variable $y = Tx$ and $d\mu(T^{-1}(X)) = d\mu(X)$, we have

$$\int_X \phi(y) \overline{\psi(y)} d\mu(y) = \langle \phi, \psi \rangle. \quad (20)$$

A more interesting way to prove the unitarity of \mathcal{G} comes from the perspective of quantum mechanics (Gyamfi, 2020). In measure-conserving systems, the Liouville operator is skew-Hermitian (as seen in the discussion of the Liouville operator and Poisson brackets in (Karasev et al., 2012)), which implies that the operator \mathcal{G} is unitary.

C.4 PROOF OF 3.3

Fact from 3.2 - the MPT property of T implies the isometric transformation as $\|\phi\|_2 = \|\phi \circ T\|_2$ for all $\phi \in \mathcal{L}^2$.

This convergence of MPT can be proved by the coboundary property⁷ such that the function ϕ can be set as $\phi = \psi - \psi \circ T$ (both $\phi, \psi \in \mathcal{L}^2$) (such function ψ can be regarded as transfer function from the perspective of cohomology in Tao (2008b)), this is easy to see

$$\begin{aligned} & \lim_{N \rightarrow \infty} \left\| \frac{1}{N} \sum_{k=0}^{N-1} \phi \circ T^k \right\|_2 \\ &= \lim_{N \rightarrow \infty} \left\| \frac{1}{N} \sum_{k=0}^{N-1} (\psi \circ T^{k-1} - \psi \circ T^k) \right\|_2 \\ &= \lim_{N \rightarrow \infty} \frac{1}{N} \|\psi - \psi \circ T^{N-1}\|_2 \\ &\leq \lim_{N \rightarrow \infty} \frac{2}{N} \|\psi\|_2 \rightarrow 0. \end{aligned} \quad (21)$$

Consequently,

$$\lim_{N \rightarrow \infty} \frac{1}{N} \sum_{k=0}^{N-1} \mathcal{G}^k \phi \rightarrow \bar{\phi}. \quad (22)$$

Thus it derived if holds for the element of subspace $\{\psi - \psi \circ T \mid \psi \in \mathcal{L}^2\}$. Then by the analysis tricks, choose a arbitrary function $\chi \in \{\psi - \psi \circ T \mid \psi \in \mathcal{L}^2\}$ satisfying $\|\chi - \phi\|_2 < \epsilon$. For the sufficiently large N we have

$$\begin{aligned} \lim_{N \rightarrow \infty} \left\| \frac{1}{N} \sum_{k=0}^{N-1} \phi \circ T^k \right\|_2 &\leq \lim_{N \rightarrow \infty} \left\| \frac{1}{N} \sum_{k=0}^{N-1} (\phi - \chi) \circ T^k \right\|_2 + \left\| \frac{1}{N} \sum_{k=0}^{N-1} \chi \circ T^k \right\|_2 \\ &\leq \lim_{N \rightarrow \infty} \left\| \frac{1}{N} \sum_{k=0}^{N-1} (\phi - \chi) \circ T^k \right\|_2 + \epsilon < 2\epsilon \end{aligned} \quad (23)$$

The proof of the first part is completed.

⁷**Coboundary of a dynamical system.** This concept is developed from cohomology theory (an interesting interpretation can be found in (Tao, 2008b)). Two functions $f, g : X \rightarrow \mathbb{C}$ are said to be cohomology via a transfer function h , if $f = g + h - h \circ T$. A function which is cohomologous to zero is called a coboundary.

In particular, $\bar{\phi}$ is invariant. If T is ergodic, $\bar{\phi}$ must be constant and $\bar{\phi} = \int \bar{\phi} d\mu$ almost surely. Also, since $\lim_{N \rightarrow \infty} \frac{1}{N} \sum_{k=0}^{N-1} \mathcal{G}^k \phi \rightarrow \bar{\phi}$, we have

$$\int \phi d\mu = \lim_{N \rightarrow \infty} \frac{1}{N} \sum_{k=0}^{N-1} \langle 1, \phi \circ T^k \rangle = \langle 1, \lim_{N \rightarrow \infty} \frac{1}{N} \sum_{k=0}^{N-1} \phi \circ T^k \rangle \rightarrow \langle 1, \bar{\phi} \rangle \rightarrow \int \bar{\phi} d\mu \quad (24)$$

The proof is different from the original proof in Neumann (1932b), Von Neumann started the proof by factorizing the spectrum using Fourier analysis and Borel functional calculus and derived the only non-trivial invariant subspaces are those consisting of constant functions.

D ANALYSIS ON OPERATOR

Contraction and unitary operators in Hilbert spaces are key tools for predicting and understanding chaotic systems in this paper. To make our work self-contained, we will provide a clear and formal analysis of these two important types of operators. Generally, the analysis on the one-parameter group is on Banach space. Since our paper is specifically defined on \mathcal{L}^2 space, we restrict our definitions and analysis to Hilbert space.

Definition D.1 (C_0 -semigroup (Engel et al., 2000)) *A strongly continuous one-parameter semigroup on a Hilbert space \mathcal{L}^2 is a family $\mathcal{G} = \{\mathcal{G}(t) \mid t \in \mathbb{R}_+\}$ of bounded linear operators $\mathcal{G}(t)$ on \mathcal{L}^2 satisfying*

- $\mathcal{G}(0) = I_d$, (the identity operator on \mathcal{L}^2)
- $\forall t, s \in \mathbb{R}_+ : \mathcal{G}(t + s) = \mathcal{G}(t)\mathcal{G}(s)$,
- $\lim_{t \rightarrow t_0} \mathcal{G}(t)\phi = \mathcal{G}(t_0)\phi$ for $t_0 \in \mathbb{R}_+$, $\phi \in \mathcal{L}^2$.

The first two axioms are algebraic, and state that \mathcal{G} is a representation of the semigroup $(\mathbb{R}_+, +)$; the last is topological, and states that the map \mathcal{G} is continuous in the strong operator topology.

If, in addition, $\|\mathcal{G}(t)\| \leq 1$ for all $t \in \mathbb{R}_+$, then \mathcal{G} is called a strongly continuous one-parameter semigroup of contractions (or contraction operator).

In our paper, our target is to learn continuous linear operators on Hilbert space, which belong to C_0 -semigroup.

Definition D.2 (Infinitesimal Generator (Engel et al., 2000)) *The infinitesimal generator of a strongly continuous one-parameter semigroup is the linear operator P on \mathcal{L}^2 defined by*

$$P\phi = \lim_{t \rightarrow 0} \frac{1}{t}(\mathcal{G}(t) - I_d)\phi, \quad (25)$$

$$\mathcal{D}(P) = \{\phi \in \mathcal{L}^2 \mid \lim_{t \rightarrow 0} \frac{1}{t}(\mathcal{G}(t) - I_d)\phi \text{ exists}\}.$$

The strongly continuous semigroup $\mathcal{G}(t)$ with generator P is often denoted by the symbol e^{tP} . This notation is compatible with the notation of matrix exponentials. Generally, directly approximating the operator P is more difficult than the operator \mathcal{G} , since operator P is usually unbounded and is defined on a dense subspace of \mathcal{L}^2 , see the following proposition.

Proposition D.3 ((Schmüdgen, 2012)) *The infinitesimal generator P is a densely defined closed operator on \mathcal{L}^2 which determines the strongly continuous one-parameter semigroup \mathcal{G} uniquely. We have*

$$\frac{d}{dt}\mathcal{G}(t)\phi = P\mathcal{G}(t)\phi, \quad \phi \in \mathcal{D}(P) \text{ and } t \in \mathbb{R}_+. \quad (26)$$

D.1 THEORETICAL ASPECTS OF KOOPMAN OPERATOR

The Koopman operator $\mathcal{G}(t)$ (Koopman, 1931; Das et al., 2021; Ikeda et al., 2022) acts on a function space by composing with the forward map T (also known as the flow map), effectively implementing time shifts in the function ϕ . Various choices exist for the function space, such as \mathcal{L}^2 and spaces of continuous functions. Specifically, for a function $\phi \in \mathcal{L}^2$ and time $t \in \mathbb{R}$, the Koopman operator $\mathcal{G}(t) : \mathcal{L}^2 \rightarrow \mathcal{L}^2$ is defined as:

$$\mathcal{G}(t)\phi = \phi \circ T. \quad (27)$$

According to Definition D.1, $\mathcal{G}(t)$ forms a semigroup.

In general, if T is a C^{k8} flow for some $k \geq 0$, then $\mathcal{G}(t)$ maps the space C^r into itself for every $0 \leq r \leq k$. The infinitesimal generator P of the Koopman operator $\mathcal{G}(t)$ is defined by:

$$Pg := \lim_{t \rightarrow 0} \frac{1}{t}(\mathcal{G}(t)\phi - \phi), \quad \phi \in \mathcal{D}(P), \quad (28)$$

⁸ C^k denotes the function space with k -th order differentiability.

where $\mathcal{D}(P) \subseteq C^1 \cap \mathcal{L}^2$ is the domain of P , consisting of functions for which this limit exists. Typically, $P : C^1 \cap \mathcal{L}^2 \rightarrow C^0 \cap \mathcal{L}^2$ when T is smooth. However, merely considering the semigroup property of the Koopman operator is insufficient for modeling the complex behavior of dissipative chaotic systems. To account for the intrinsic physical properties of such systems, we incorporate this physical knowledge into the learning framework. Specifically, we analyze two intrinsic physical properties from spectral theory—contraction and unitarity—as detailed in Section D.4 and Appendix D.3.

D.2 CONTRACTION OPERATOR ON HILBERT SPACE

Definition D.4 ((Schmüdgen, 2012)) We shall say that the operator B is accretive if $\operatorname{Re}(\langle B\phi, \phi \rangle) \geq 0$ for all $\phi \in \mathcal{D}(B)$ that B is m -accretive if B is closed, accretive, and $R(B - \lambda_0 I)$ is dense in \mathcal{L}^2 for some $\lambda_0 \in \mathbb{C}$, $\operatorname{Re}(\lambda_0) < 0$ ⁹.

B is called dissipative if $-B$ is accretive and m -dissipative if $-B$ is m -accretive.

Theorem D.5 (Lumer–Phillips theorem in Hilbert space) A linear operator P on a Hilbert space \mathcal{L}^2 is the generator of a strongly continuous one-parameter contraction semigroup if and only if P is m -dissipative, or equivalently, $-P$ is m -accretive.

Proof. If P is the generator of a contraction semigroup \mathcal{G} , then in particular P is dissipative, and hence $\operatorname{Re}(\langle P\phi, \phi \rangle) \leq 0$ for $\phi \in \mathcal{L}^2$ by D.4. Thus, the latter fact can be easily derived directly. Indeed, using that $\mathcal{G}(t)$ is a contraction in D.1, we obtain

$$\operatorname{Re}(\langle (\mathcal{G}(t) - I_d)\phi, \phi \rangle) = \operatorname{Re}(\langle \mathcal{G}(t)\phi, \phi \rangle) - \|\phi\|^2 \leq \|\mathcal{G}(t)\phi\| \|\phi\| - \|\phi\|^2 \leq 0 \quad (29)$$

Dividing by $t \rightarrow 0$ and passing to the limit $t \rightarrow 0^+$, we get $\langle P\phi, \phi \rangle \leq 0$.

Combining the D.3 and D.5 states the eigenvalues of infinitesimal generator $P := \lim_{t \rightarrow 0^+} \frac{\mathcal{G}_t \phi - \phi}{t}$ of contraction operator \mathcal{G} has non-positive real parts. However, the operator P is usually unbounded and is defined on a dense subspace of \mathcal{L}^2 (Engel et al., 2000). Directly learning the infinitesimal generator P can be more difficult than working with operator \mathcal{G} . To simplify the problem, we can consider eigenvalues of \mathcal{G} within the unit disk in the complex plane during the contraction stage see Equation 6.

Spectral Analysis on $\mathcal{G}^T \mathcal{G}$. We define the operator norm as $\|\mathcal{G}\| := \sup_{\phi \in \mathcal{L}^2} \|\mathcal{G}\phi\|_2$. Given that \mathcal{G} is contraction, we know

$$\|\mathcal{G}\| \leq 1 \quad \Rightarrow \quad \|\mathcal{G}^T \mathcal{G}\| \leq \|\mathcal{G}\|^2 \leq 1. \quad (30)$$

Since $\mathcal{G}^T \mathcal{G}$ is a positive operator (because $\mathcal{G}^T \mathcal{G}$ is self-adjoint and non-negative), the norm $\|\mathcal{G}^T \mathcal{G}\|$ is equal to the spectral radius of $\mathcal{G}^T \mathcal{G}$, and hence

$$\sigma(\mathcal{G}^T \mathcal{G}) \subset [0, \|\mathcal{G}^T \mathcal{G}\|] \subset [0, 1]. \quad (31)$$

This show that $\mathcal{G}^T \mathcal{G}$ is also a contraction operator, since $\|\mathcal{G}^T \mathcal{G}\| \leq 1$.

D.3 UNITARY OPERATOR

Definition D.6 (Unitary Operator (Schmüdgen, 2012)) A strongly continuous one-parameter unitary group briefly a unitary group, is a family $\mathcal{G} = \{\mathcal{G}(t) \mid t \in \mathbb{R}\}$ of unitaries $\mathcal{G}(t)$ on Hilbert space \mathcal{L}^2 such that

- $\mathcal{G}(t)\mathcal{G}(s) = \mathcal{G}(t+s)$ for all $t, s \in \mathbb{R}$,
- $\lim_{h \rightarrow 0} \mathcal{G}(t+h)\phi = \mathcal{G}(t)\phi$ for $\phi \in \mathcal{L}^2$ and $t \in \mathbb{R}$.

Axiom (i) in D.6 means that \mathcal{G} is group homomorphism of the additive group \mathbb{R} into the group of unitary operators on \mathcal{L}^2 . In particular, this implies that $\mathcal{G}(0) = I_d$ and

$$\mathcal{G}(-t) = \mathcal{G}^{-1} = \mathcal{G}^* \quad \forall t \in \mathbb{R}. \quad (32)$$

⁹ $\operatorname{Re}(\cdot)$ is denoted as the real part, and $R(B)$ is the range of operator B .

Axiom (ii) in D.6 is a strong continuity of \mathcal{G} . It clearly suffices to require (ii) for $t = 0$ and for ϕ from a dense subset of \mathcal{L}^2 . Since the operators $\mathcal{G}(t)$ are unitaries, it is even enough to assume that $\lim_{t \rightarrow 0} \langle \mathcal{G}(t)\phi, \phi \rangle = \langle \phi, \phi \rangle$ for ϕ from a dense subset of \mathcal{L}^2 .

The generator P of the one-parameter unitary group $\mathcal{G}(t)$ satisfying the following relationship

$$\mathcal{G}(t) = \exp(itP) \quad \forall t \in \mathbb{R}. \quad (33)$$

The operator P governs the infinitesimal behavior of the group and is defined by the strong limit:

$$P\phi = \lim_{t \rightarrow 0} \frac{\mathcal{G}\phi - \phi}{it}, \quad (34)$$

for all ϕ in domain $\mathcal{D}(P)$ of P , which consists of those functionals for which limit exists.

Since $\mathcal{G}(t) = \exp(itP)$ where P is skew-adjoint $P^* = -P$, the spectrum of $\mathcal{G}(t)$ must lie on the unit circle.

Spectral Properties. For all $\mathcal{G}(t), t \in \mathbb{R}$, its spectrum $\sigma(\mathcal{G}(t))$ lies on the complex unit circle \mathbb{T} , which is the set of complex numbers with absolute value 1

$$\sigma(\mathcal{G}(t)) \subset \{r \in \mathbb{C} \mid |r| = 1\}.$$

Physical Interpretation of Two Operators. During the contraction phase, changes in the probability distribution inherently reflect the asymmetry of entropy with respect to time. This phenomenon is explained by the second law of thermodynamics: the contraction operator, associated with energy dissipation. However, with an invariant measure, the system's evolution is governed by a unitary operator if it satisfies the Liouville equation (in the classical setting) or the Liouville-von Neumann equation (in the quantum setting) (see B.3), which makes the density matrix or the invariant measure time-independent (Tao, 2008a), respectively. Consequently, a unitary operator and its conjugate transpose can describe the forward and backward chaotic dynamics on the invariant set.

E ALGORITHM

Algorithm 1 Poincaré Flow Neural Network

PFNN: Training

Require: Training data $\mathcal{D} = \{(s_t^i, s_{t+1}^i)\}_{t=0}^{T-1}\}_{i=0}^N$ with number of trajectories N and trajectory length T , relaxation time k , training epochs N_{train} , learning rate α , regularized coefficients γ_1, γ_2 encoder $g_{\theta_1}^{\text{en}}: \mathcal{M} \rightarrow \mathbb{R}^L$, decoder $g_{\theta_2}^{\text{de}}: \mathbb{R}^L \rightarrow \mathcal{M}$ with latent feature dimension L

- (contraction phase) operator $\hat{\mathcal{G}}_c \in \mathbb{R}^{L \times L}$
(measure invariant phase) forward operator $\hat{\mathcal{G}}_m \in \mathbb{R}^{L \times L}$, backward operator $\hat{\mathcal{G}}_m^* \in \mathbb{R}^{L \times L}$
- 1: Separate the dataset \mathcal{D} into contraction phase dataset $\mathcal{D}_c = \{(s_t^i, s_{t+1}^i)\}_{t=0}^{k-1}\}_{i=0}^N$ and measure invariant phase dataset $\mathcal{D}_m = \{(s_t^i, s_{t+1}^i)\}_{t=k}^{T-1}\}_{i=0}^N$.
 - 2: **for** training epoch $e = 1, \dots, N_{\text{train}}$ **do**
 - 3: Compute contraction loss $\mathcal{L}_{\text{contraction}}$ by Equation 6 with regularized coefficient γ_1 on \mathcal{D}_c .
 - 4: Update $\hat{\mathcal{G}}_c, \theta_1, \theta_2 \leftarrow \alpha \nabla_{\hat{\mathcal{G}}_c, \theta_1, \theta_2} \mathcal{L}_{\text{contraction}}$
 - 5: Compute measure invariant loss $\mathcal{L}_{\text{unitary}}$ by Equation 8 with regularized coefficient γ_2 on \mathcal{D}_m .
 - 6: Update $\hat{\mathcal{G}}_m, \hat{\mathcal{G}}_m^*, \theta_1, \theta_2 \leftarrow \alpha \nabla_{\hat{\mathcal{G}}_m, \hat{\mathcal{G}}_m^*, \theta_1, \theta_2} \mathcal{L}_{\text{unitary}}$
 - 7: **end for**
 - 8: **return** $g_{\theta_1}^{\text{en}}, g_{\theta_2}^{\text{de}}, \hat{\mathcal{G}}_c, \hat{\mathcal{G}}_m, \hat{\mathcal{G}}_m^*$
 - 9:

PFNN: Evaluating

- 10: Given initial condition $s_0 \in \mathcal{M}$
 - 11: **for** timestep $t = 1, \dots, k$ **do**
 - 12: Predict using $\hat{\mathcal{G}}_c, g_{\theta_1}^{\text{en}}(\hat{s}_{t+1}) = \hat{\mathcal{G}}_c g_{\theta_1}^{\text{en}}(\hat{s}_t)$
 - 13: **end for**
 - 14: Collection $\mathcal{D}_{\text{statistics}} = \{\}$
 - 15: **for** timestep $t > k$ **do**
 - 16: Predict using $\hat{\mathcal{G}}_m, g_{\theta_1}^{\text{en}}(\hat{s}_{t+1}) = \hat{\mathcal{G}}_m g_{\theta_1}^{\text{en}}(\hat{s}_t)$ and $\hat{s}_{t+1} = g_{\theta_2}^{\text{de}} \circ g_{\theta_1}^{\text{en}}(\hat{s}_{t+1})$
 - 17: $\mathcal{D}_{\text{statistics}} \cup \{\hat{s}_{t+1}\}$
 - 18: **end for**
 - 19: Estimate required long-term statistics $\{\mu, \sigma, \dots\}$ using $\mathcal{D}_{\text{statistics}}$
 - 20: **return** long-term statistics $\{\mu, \sigma, \dots\}$
-

F MORE EXPERIMENTAL RESULTS

F.1 LORENZ 63

The Lorenz 63 model (Lorenz, 1963), which consists of three coupled nonlinear ODEs,

$$\frac{dx}{dt} = \sigma(y - x), \quad \frac{dy}{dt} = x(\rho - z) - y, \quad \frac{dz}{dt} = xy - \beta z \quad (35)$$

used as a model for describing the motion of a fluid under certain conditions: an incompressible fluid between two plates perpendicular to the direction of the earth’s gravitational force. In particular, the equations describe the rate of change of three quantities with respect to time: x is proportional to the rate of convection, y to the horizontal temperature variation, and z to the vertical temperature variation. The constants σ , ρ , and β are system parameters proportional to the Prandtl number, Rayleigh number, and coupling strength. In this paper, we take the classic choices $\sigma = 10$, $\rho = 28$, and $\beta = \frac{8}{3}$ which leads to a chaotic behavior with two strange attractors $(\sqrt{\beta(\rho - 1)}, \sqrt{\beta(\rho - 1)}, \rho - 1)$ and $(-\sqrt{\beta(\rho - 1)}, -\sqrt{\beta(\rho - 1)}, \rho - 1)$. Its state is $s = (x, y, z) \in \mathbb{R}^3$ bounded up and below from ± 30 .

Lorenz 63 Components	KL Divergence				
	FNO	LSTM	Koopman	MNO	PFNN
x	0.5045	∞	0.8621	3.2241	0.2408
y	0.9339	∞	0.6975	2.6191	0.5155
z	0.3913	∞	0.4172	0.1996	0.1005

Table 3: KL Divergence for long-term prediction distributions of Lorenz 63 system

F.2 LORENZ 96

This system was introduced in (Lorenz, 1996) as a low-order model of atmospheric circulation at a constant latitude circle. The system consists of K variables $\mathbf{S} = (S_1, \dots, S_K) \in \mathcal{S} \subseteq \mathbb{R}^K$, representing the values of atmospheric velocity measured along a circle of K evenly spaced locations on the certain latitude of the earth. The governing equations are given by,

$$\frac{dS_k}{dt} = -S_{k-1}(S_{k-2} - S_{k+1}) - S_k + F, \quad (36)$$

where the parameter F represents the forcing term. Here, the first term models advection, the second term represents linear damping, and F is an external forcing. We choose the set of variables of $K = \{9, 40, 80\}$ and the external forcing $F = 8$, parameters where the system is chaotic with the Lyapunov exponent is approximately 1.67. Its dynamics exhibit strong energy-conserving non-linearity, and for a large $F \geq 10$, it can exhibit strong chaotic turbulence and symbolizes the inherent unpredictability of the Earth’s climate.

Data generation: we generated 1800 trajectories for training and 200 trajectories for testing, where each trajectory contains 2000 timesteps with integration time 0.01 and a sample rate of 10. Meanwhile, in the best alignment with real scenarios, the initial conditions for trajectories in the training and testing set were drawn from a normal distribution.

Experiment setup: for PFNN models, when training the PFNN (consist) model, we discarded the initial 1000 timesteps to avoid the dissipative process; whilst for training the PFNN (contract) model, the initial steps were maintained to specialize the model in learning the dissipativity in the early-stage emulation. For all other models, the initial 100 timesteps were discarded. In the model prediction part, the PFNN (full) model autoregressively predicted the system states with the PFNN (contract) model for the beginning 900 timesteps, and then switched to PFNN (consist) model to predict the states for the rest 1000 timesteps. For all other models, the trajectory for 1900 timesteps was predicted in the same autoregressive way.

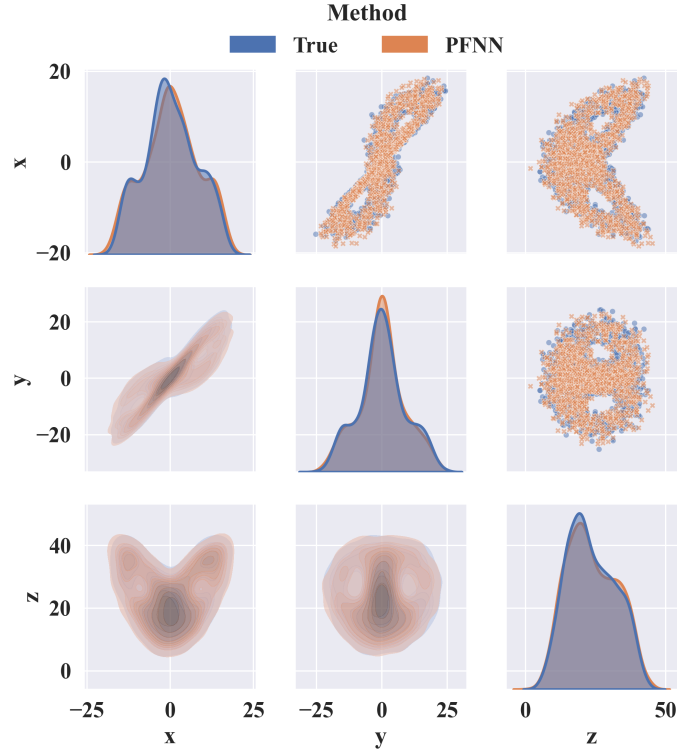


Figure 4: Visualization of long-term statistics of model predictions for Lorenz 63 system of 3 dimensions: we visualize the spatial correlation among 3 components of the velocity, focusing on evaluating the learnt spatial correlation from the PFNN model’s long-term predictions compared with the ground truth.

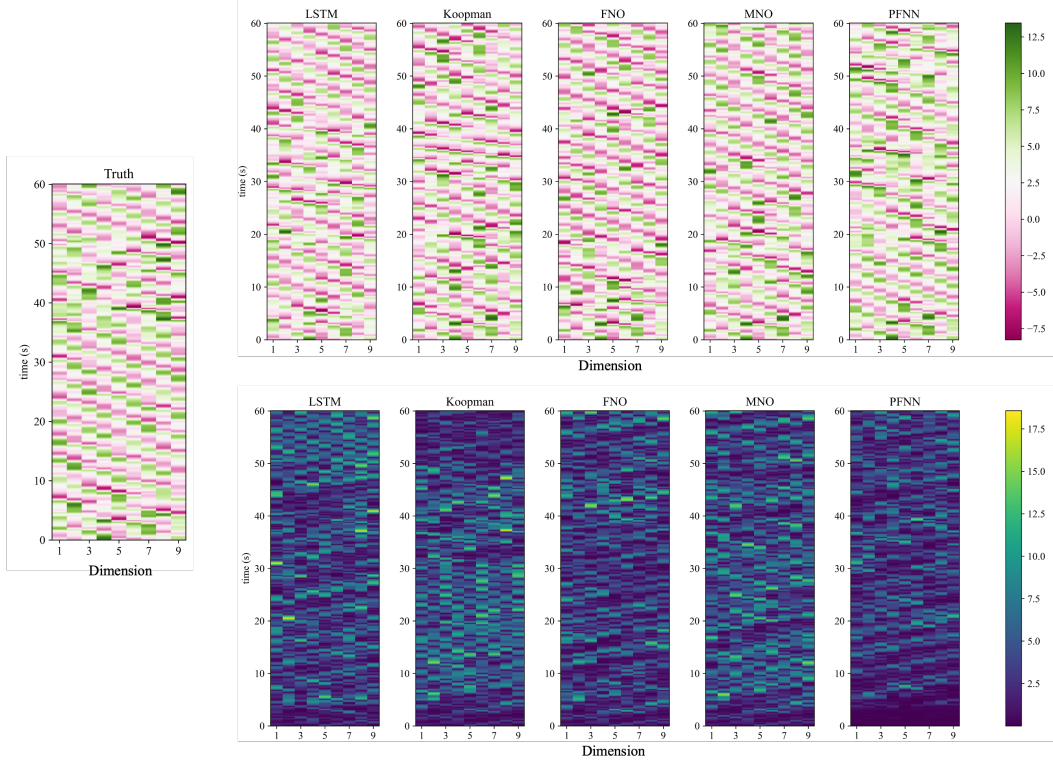
F.2.1 EXPERIMENT ON 9 DIMENSIONAL DATASET

Contents:

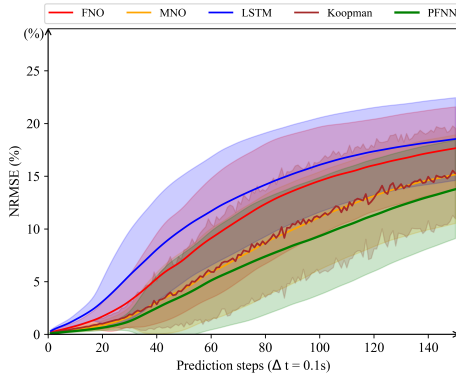
- Table of KL divergence (Table 4)
- Short-term prediction plot set (Figure 5)
- Long-term prediction plot set (Figure 6)

Principle Components (PC)	KL Divergence				
	FNO	LSTM	Koopman	MNO	PFNN
PC1	2.7491	2.2425	2.1491	1.8512	1.5920
PC2	2.5773	2.6774	2.1152	2.1392	1.9539
PC3	2.4614	5.5756	2.1090	2.1616	2.0637

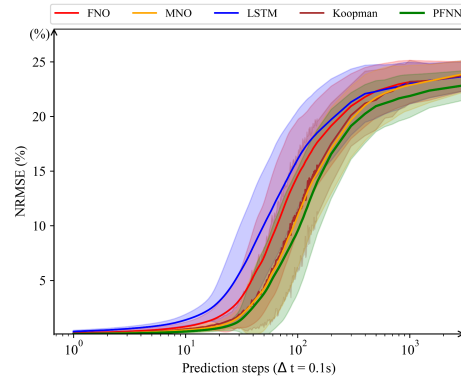
Table 4: KL Divergence for long-term prediction distributions by models across 3 principal components of Lorenz 96 system of 9-dimensional states



(a) Prediction visualization. The ground truth trajectory is visualized in the middle of the leftmost side. The predicted trajectories by baseline models and PFNN are shown in the first row. The corresponding absolute error trajectories of the predictions against the ground truth are shown in the second row.

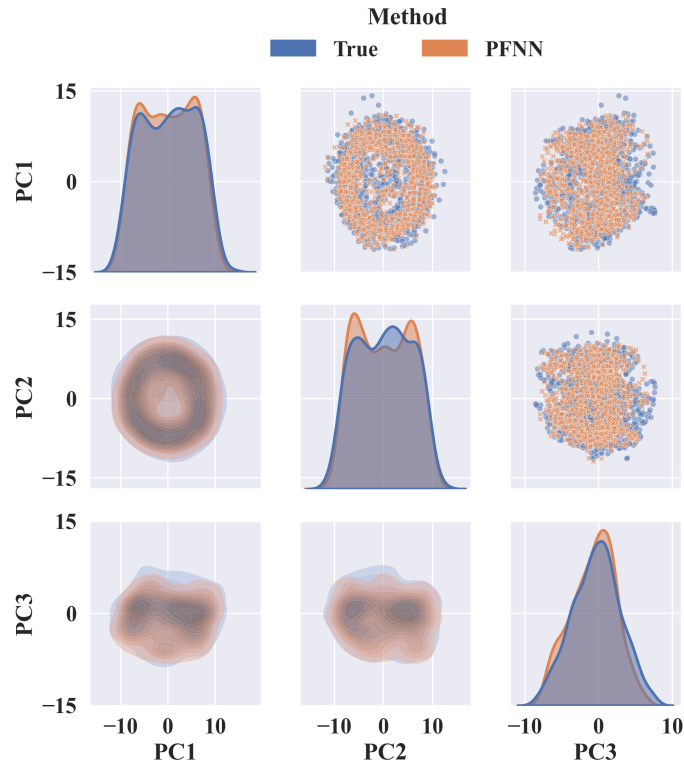


(b) Accuracy of prediction over 15s.



(c) Accuracy of prediction over 100s.

Figure 5: Visualization of prediction error in NRMSE: we visualize the comparison of model predictions of Lorenz 96 dynamics of 9 dimensions over 15 seconds (150 timesteps, short-term) and 100 seconds (1000 timesteps, mid-term).



(a) Spatial correlation of PFNN in 3 principle components

Figure 6: Visualization of long-term statistics of model predictions for Lorenz 96 of 9 dimensions: we visualize the spatial correlation among 3 principle components of the velocity, focusing on evaluating the learnt spatial correlation from the PFNN model’s long-term predictions compared with the ground truth.

F.2.2 EXPERIMENT ON 40 DIMENSIONAL DATASET

Contents:

- Table of KL divergence (Table 5)
- Short-term prediction plot set (Figure 7)
- Long-term prediction plot set (Figure 8)

Principle Components (PC)	KL Divergence				
	FNO	LSTM	Koopman	MNO	PFNN
PC1	0.1427	62659.3087	0.1323	0.1654	0.0497
PC2	0.0987	62822.3591	0.0784	0.1309	0.0356
PC3	0.0767	64132.3089	0.0575	0.1755	0.1015
PC4	0.1309	63519.8891	0.1572	0.1982	0.797
PC5	0.1305	62346.3862	0.1247	0.1106	0.0556

Table 5: KL Divergence for long-term prediction distributions by models across 5 principal components of Lorenz 96 system of 40-dimensional states

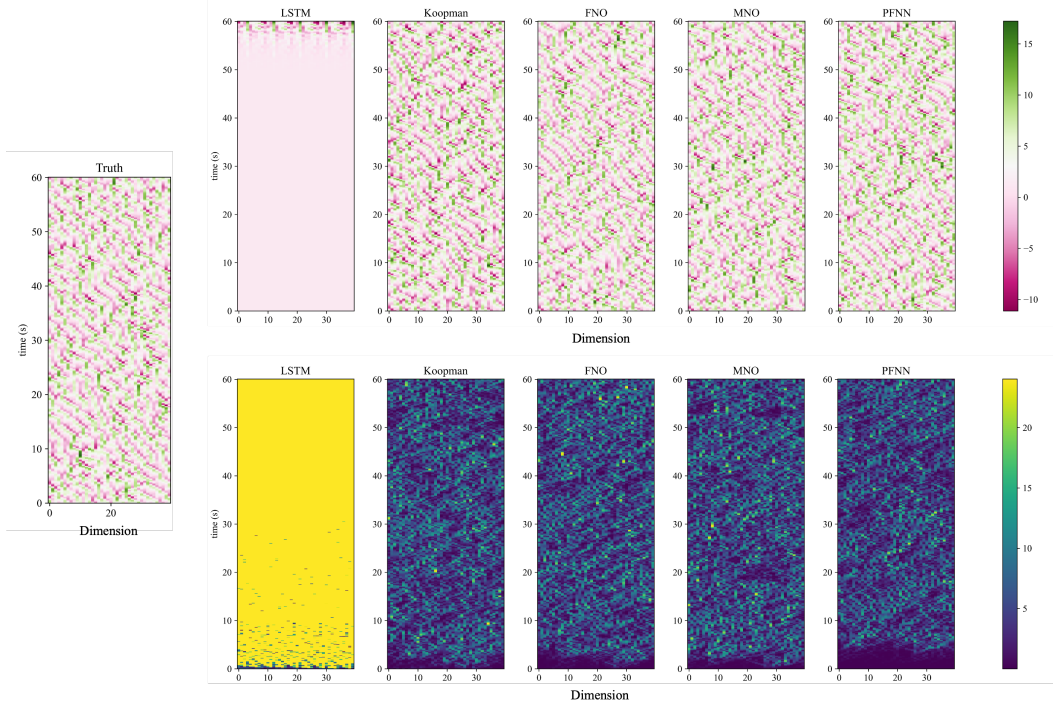
F.2.3 EXPERIMENT ON 80 DIMENSIONAL DATASET

Contents:

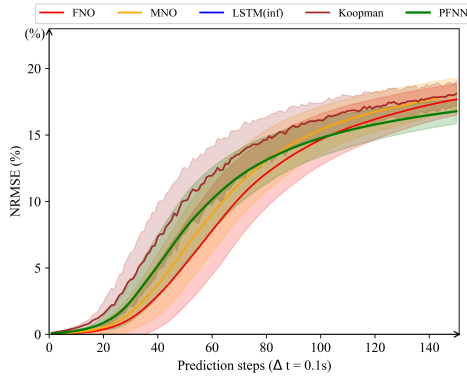
- Table of KL divergence (Table 6)
- Short-term prediction plot set (Figure 9)
- Long-term prediction plot set (Figure 10)

Principle Components (PC)	KL Divergence				
	FNO	LSTM	Koopman	MNO	PFNN
PC1	0.0785	1.3057	0.1650	0.2384	0.0733
PC2	0.1345	1.3413	0.2477	0.2268	0.0801
PC3	0.1746	1.4145	0.1613	0.0574	0.0524
PC4	0.1900	1.2329	0.2324	0.0394	0.1220
PC5	0.2651	1.2965	0.3733	0.3391	0.1724

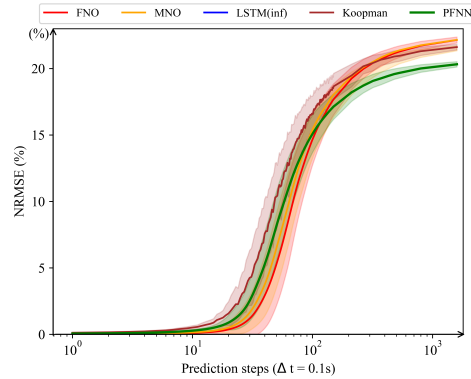
Table 6: KL Divergence for long-term prediction distributions by models across 5 principal components of Lorenz 96 system of 80-dimensional states



(a) Prediction visualization. The ground truth trajectory is visualized in the middle of the leftmost side. The predicted trajectories by baseline models and PFNN are shown in the first row. The corresponding absolute error trajectories of the predictions against the ground truth are shown in the second row.

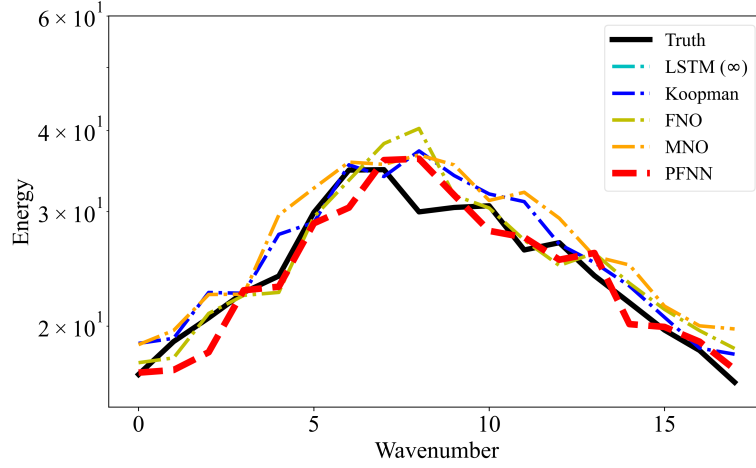


(b) Accuracy of prediction over 15s.

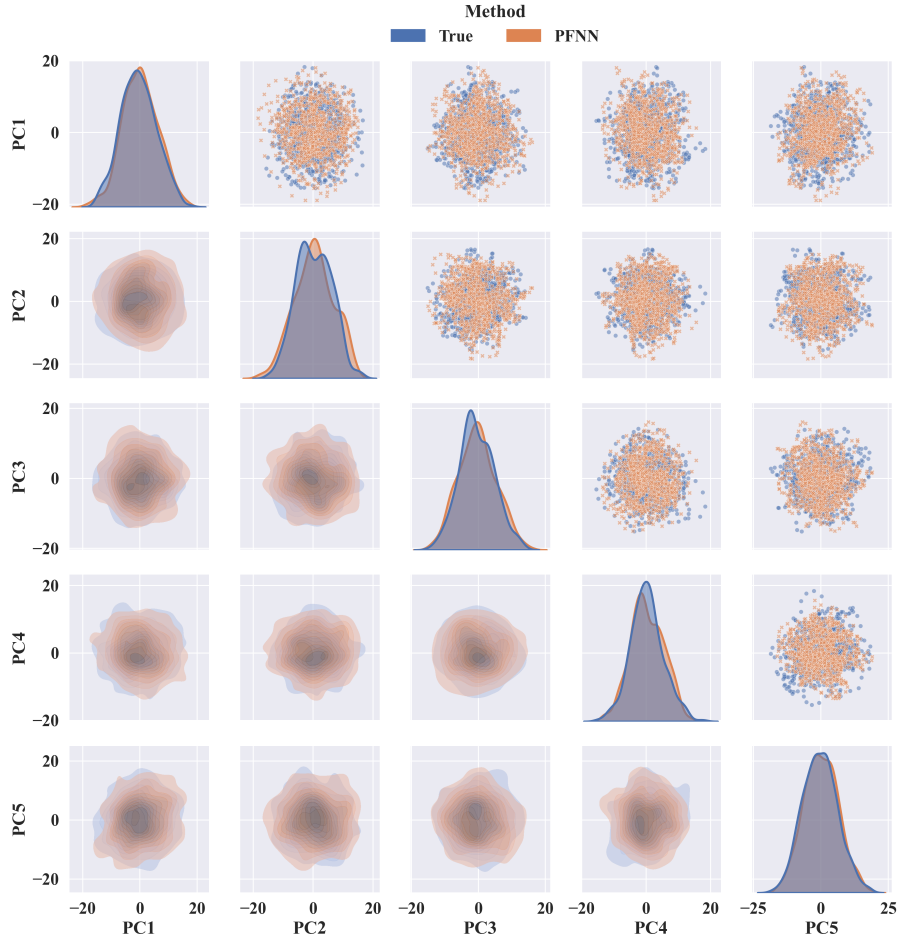


(c) Accuracy of prediction over 100s.

Figure 7: Visualization of prediction error in NRMSE: we visualize the comparison of model predictions of Lorenz 96 dynamics of 40 dimensions over 15 seconds (150 timesteps, short-term) and 100 seconds (1000 timesteps, mid-term).

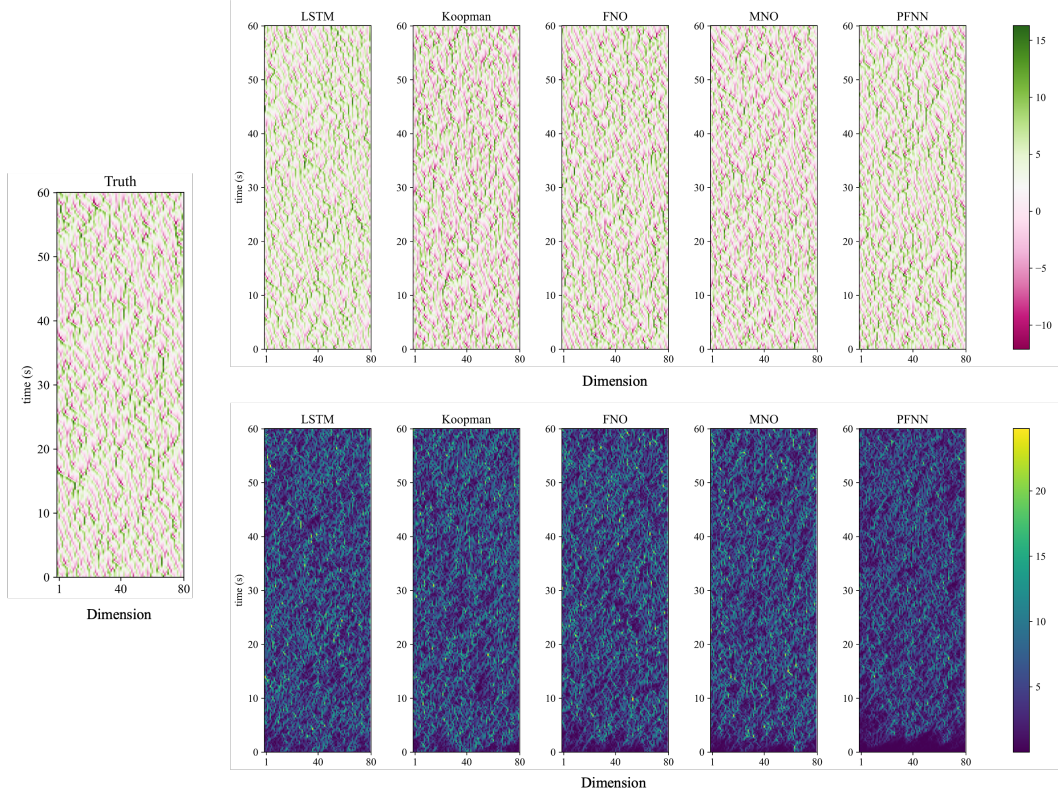


(a) Energy spectrum of velocity

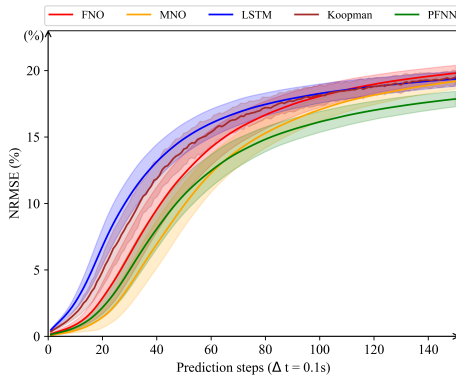


(b) Spatial correlation of PFNN in 5 principle components

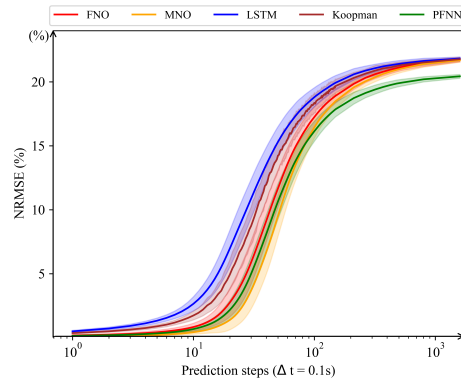
Figure 8: Visualization of long-term statistics of model predictions for Lorenz 96 system of 40 dimensions: we visualize density plots of each state dimension of the system velocity predicted by all six models; and then we visualize the spatial correlation among 5 principle components of the velocity, focusing on evaluating the learnt spatial correlation from the PFNN model’s long-term predictions compared with the ground truth.



(a) Prediction visualization. The ground truth trajectory is visualized in the middle of the leftmost side. The predicted trajectories by baseline models and PFNN are shown in the first row. The corresponding absolute error trajectories of the predictions against the ground truth are shown in the second row.

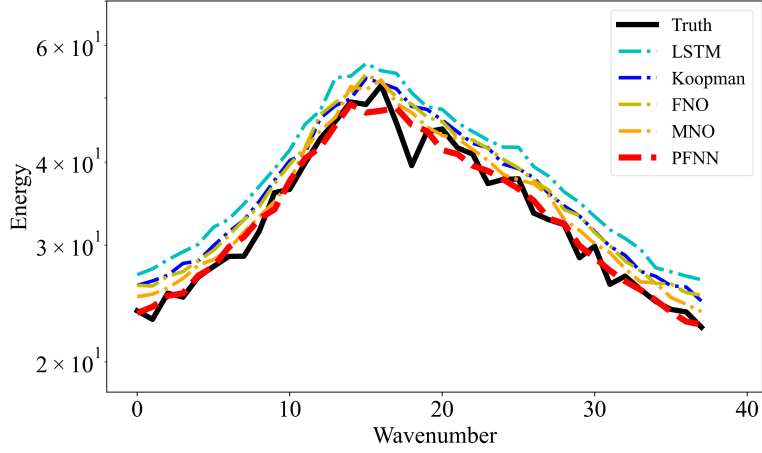


(b) Accuracy of prediction over 15s.

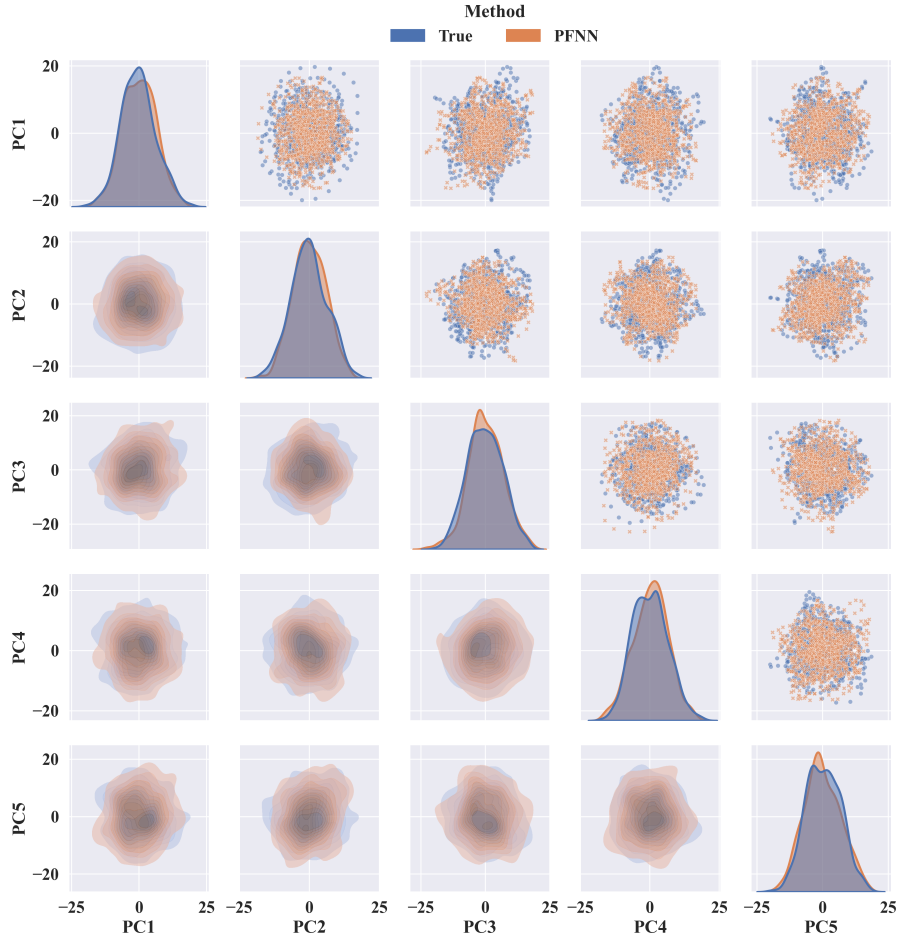


(c) Accuracy of prediction over 100s.

Figure 9: Visualization of prediction error in NRMSE: we visualize the comparison of model predictions of Lorenz 96 dynamics of 80 dimensions over 15 seconds (150 timesteps, short-term) and 100 seconds (1000 timesteps, mid-term).



(a) Energy spectrum of velocity



(b) Spatial correlation of PFNN in 5 principle components

Figure 10: Visualization of long-term statistics of model predictions for Lorenz 96 system of 80 dimensions: we visualize density plots of each state dimension of the system velocity predicted by all six models; and then we visualize the spatial correlation among 5 principle components of the velocity, focusing on evaluating the learnt spatial correlation from the PFNN model’s long-term predictions compared with the ground truth.

F.3 KURAMOTO-SIVASHINSKY

The Kuramoto-Sivashinsky (KS) equation (Papageorgiou & Smyrlis, 1991), well-known for its chaotic behavior, is a nonlinear PDE applied to studying pattern formation and instability in fluid dynamics, combustion, and plasma physics. The dynamics in 1d spatial domain $u(x, t)$ is given by

$$\frac{\partial u}{\partial t} + u \frac{\partial u}{\partial x} + \frac{\partial^2 u}{\partial x^2} + \frac{\partial^4 u}{\partial x^4} = 0, \quad (37)$$

where $x \in [0, L]$ with a periodic boundary condition. The interaction of high-order terms produces complex spatial patterns and temporal chaos when the domain length L is large enough (Cvitanović et al., 2010).

Dataset processing for training and testing: The dataset of Kuramoto-Sivashinsky simulations we utilized was obtained from the public source, consisting of 1200 simulated trajectories with 512 spatial dimensions, $u(x, t)$, on the periodic boundary. The simulations employed a pseudo-spectral method with exponential time differencing (ETD) to evolve the dynamics. Each trajectory was generated over 2000 timesteps with integration time $0.005s$ and sample rate of 10. We sampled 128-dimensional u and used 1000 trajectories for training and 200 trajectories for testing, where each trajectory was truncated to 1990 timesteps to preserve the contraction phase before the system reached the ergodic state. For model training, the full trajectory length (1990 timesteps) was used to train baseline models, while the trajectory before the contraction step k was used to train the PFNN contraction operator \hat{G}_c , and the trajectory after k was used to train the PFNN measure-invariant operators \hat{G}_c and \hat{G}_m^* . The determination of the contraction step k via the ablation study can be found in Table 10. For model evaluation, the full trajectory length in the test set was applied to all models.

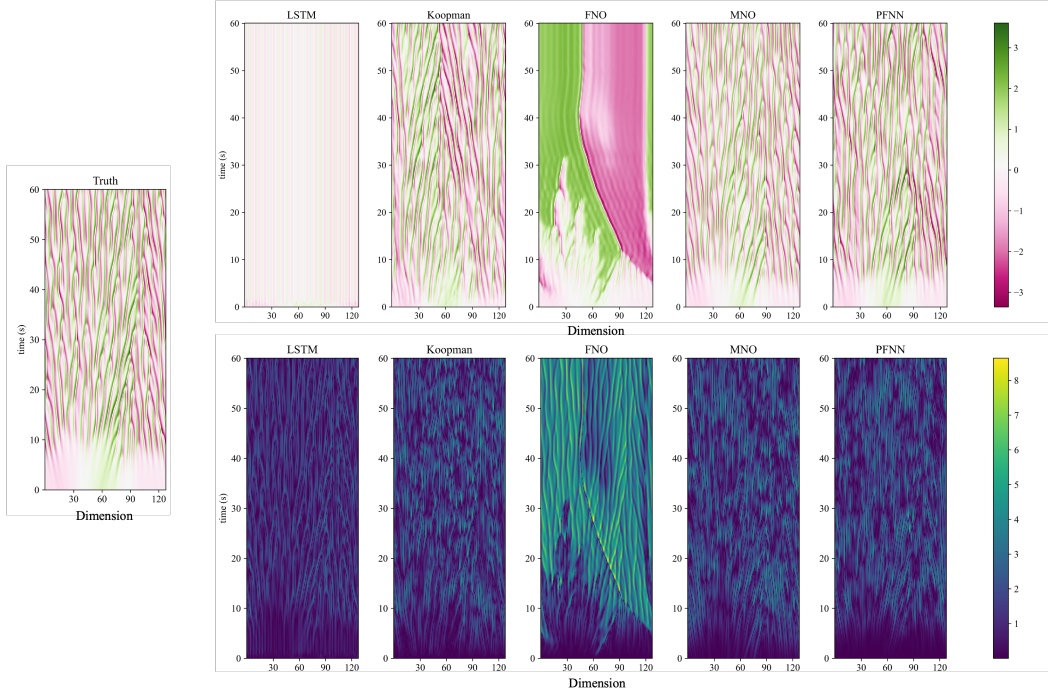
PFNN model architecture: The PFNN model is designed to incorporate three pairs of encoder-decoder layers: one operator layer to represent the contraction dynamics, and two operator layers to represent unitary characteristics in the measure-invariant forward and backward dynamics. The model is implemented with PyTorch version 2.3.1, and the details of the layers are presented in Table 8.

Benchmarks for Kuramoto-Sivashinsky: We compare the PFNN model with classic recurrent neural networks: the Long Short-Term Memory network (LSTM), Koopman Operator network, Fourier Neural Operator (FNO), and Markov Neural Operator (MNO). We use the Adam optimizer to minimize the relative L2 loss with a learning rate of $1e-4$, and a step learning rate scheduler that decays by half every 10 epochs, for a total of 100 epochs. Based on the provided code source in Appendix G, (1) for LSTM, we chose 2 layers and a latent feature dimension of 2×128 ; (2) for the Koopman Operator, we chose 1 layer and a latent feature dimension of 4×128 ; (3) for FNO and MNO, we set the width to 40, considering the down-sampled state dimension, and chose 30 Fourier modes to improve their ability to learn high-frequency dynamics; (4) for PFNN, the latent feature dimension is 8×128 for both the contraction model and the measure-invariant model.

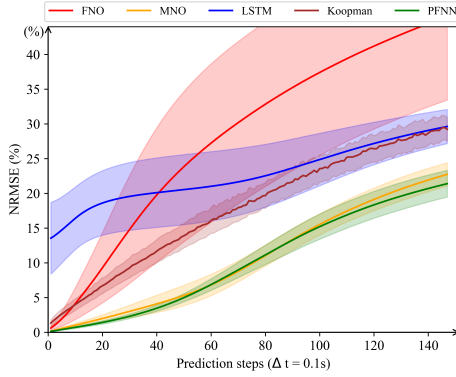
Principle Components (PC)	KL Divergence				
	FNO	LSTM	Koopman	MNO	PFNN
PC1	143.6508	∞	40.6045	27.8991	11.2828
PC2	133.1811	∞	43.0569	40.6271	14.8646
PC3	137.7399	∞	40.6242	31.9322	6.6711
PC4	122.4125	∞	29.3022	33.4713	4.6851
PC5	176.6664	∞	108.9509	33.7227	9.3462

Table 7: KL Divergence for long-term prediction distributions by models across principal components of Kuramoto-Sivashinsky

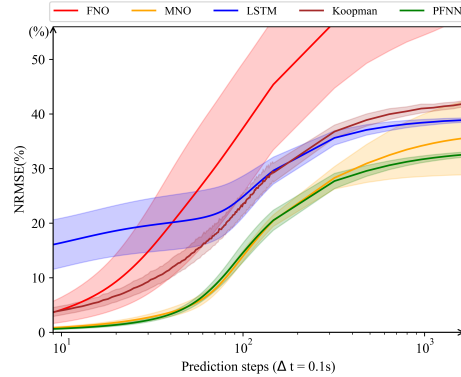
Accuracy results: we provide more short-term and mid-term accuracy evaluations in 11. We noted Figure Notes: Visualization of model prediction performance from the NRMSE of short-term prediction to relevant statistics of long-term prediction. We used 200 test samples and plotted the mean and standard deviation of all test results to obtain the NRMSE of the prediction.



(a) Prediction visualization. The ground truth trajectory is visualized in the middle of the leftmost side. The predicted trajectories by baseline models and PFNN are shown in the first row. The corresponding absolute error trajectories of the predictions against the ground truth are shown in the second row.

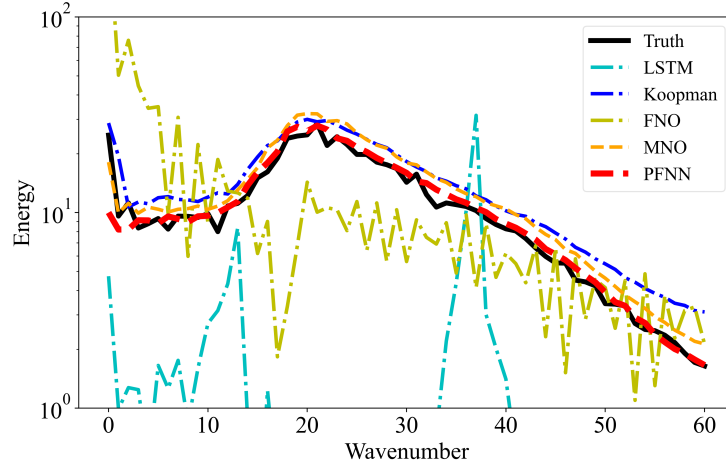


(b) Accuracy of prediction over 15s.

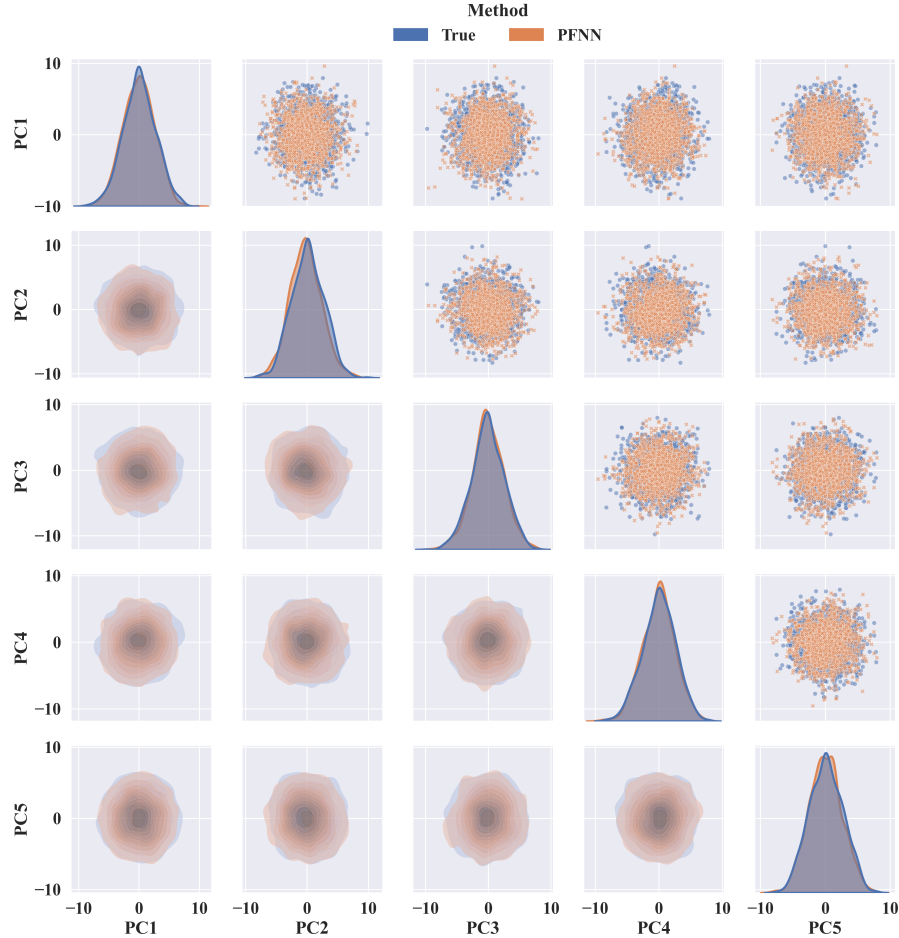


(c) Accuracy of prediction over 100s.

Figure 11: Visualization of prediction error in NRMSE: we visualize the comparison of model predictions of Kuramoto-Sivashinsky dynamics over 15 seconds (150 timesteps, short-term) and 100 seconds (1000 timesteps, mid-term).



(a) Energy spectrum of velocity



(b) Spatial correlation of PFNN in 5 principle components

Figure 12: Visualization of long-term statistics of model predictions for Kuramoto-Sivashinsky: we visualize the energy spectrum of model predictions over 64 wavenumbers; and then we visualize the spatial correlation among 5 principle components of PFNN long-term predictions over all test states comparing with the spectrum of the ground truth.

F.4 KOLMOGOROV FLOW

The Kolmogorov flow system, introduced by Arnold Kolmogorov, is a classic model for studying fluid instabilities and turbulence in two-dimensional incompressible flows Temam (2012). It is described by a nonlinear, incompressible Navier-Stokes equation driven by a sinusoidal forcing term.

$$\frac{\partial \mathbf{u}}{\partial t} + (\mathbf{u} \cdot \nabla) \mathbf{u} + \nabla p - \frac{1}{Re} \nabla^2 \mathbf{u} - \sin(kx) \hat{\mathbf{y}} = 0, \quad (38)$$

where $\mathbf{u}(x, y, t)$ is the velocity field, p is the pressure, ν is the kinematic viscosity, and $\sin(kx) \hat{\mathbf{y}}$ represents the external forcing in the y -direction. The experiment setting follows the (Alieva et al., 2021).

PFNN model architecture: The PFNN model for the 2-D task begins with Convolution2D layers to do patch embedding of the input state, and employs the attention mechanism within Transformer Blocks Dosovitskiy et al. (2021) to perform feature encoding. Then, one operator layer is used to learn the contraction dynamics; and two operator layers are used to learn the unitary characteristics in the measure-invariant forward and backward dynamics. The model is implemented with PyTorch version 2.3.1, with detailed layer configurations provided in Table 9.

Short-term prediction accuracy: We compared the model performance in the short-term forecasting accuracy by evaluating the absolute error of model predictions with the true states at timesteps 2, 4, 8, 16 and 32 in measure-invariant phase in Figure 13. The result showed PFNN exhibits the smallest error across all steps, closely matching the ground truth and maintaining low errors even at Step 32. We further evaluated the turbulent kinetic energy, which is defined as:

$$TKE = \frac{1}{2} (\overline{u'^2} + \overline{v'^2}) \quad (39)$$

where u', v' are the fluctuating components of velocity compared to velocity mean over time in the x and y directions respectively. The TKE measure in Figure 14 demonstrates that the PFNN results outperform other baseline models.

Estimating statistics in equilibrium: We compared PFNN predicted trajectories with other model predicted trajectories and the true trajectories in Figure 3. The result showed PFNN predicted trajectory preserved the internal physics statistics in (a) reproducing the turbulent kinetic energy distribution; and (b) capturing the time-average state of a system in equilibrium. Plot (c) showed that the PFNN predicted trajectory had the lowest absolute error (AE) of the predicted mean state against the true mean state.

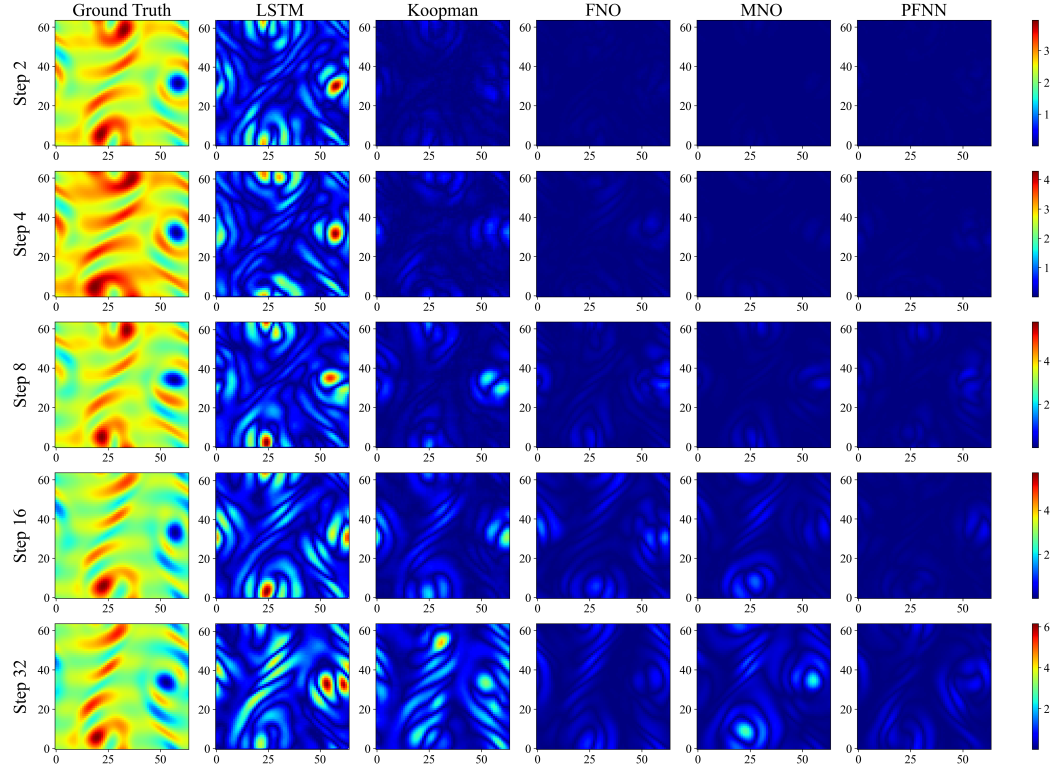


Figure 13: Visualization of the absolute difference of model predictions from ground truth in short-term steps $\{2, 4, 8, 16, 32\}$.

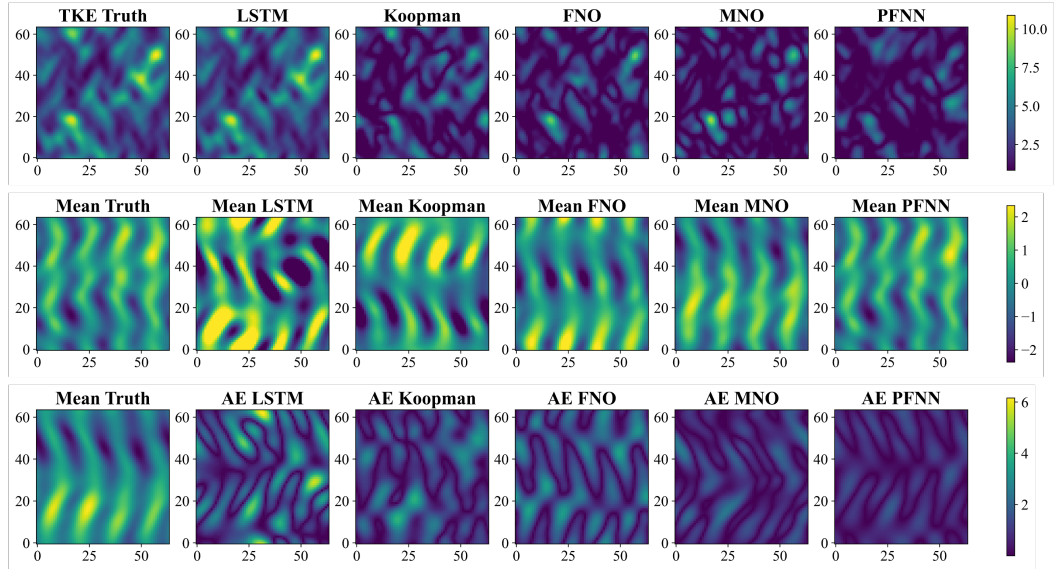


Figure 14: Visualization of the forecast trajectory sample of Kolmogorov Flow system in **top row**: the turbulent kinetic energy, which illustrates the accuracy of model predictions in reproducing the kinetic energy distribution; **middle row**: the mean state that demonstrated each model's ability in capturing the time-average velocity field of a system in equilibrium, where plot **bottom row**: the absolute error (AE) outstands the difference the predicted mean state against the true mean state.

G EXPERIMENT SETTINGS

G.1 NEURAL NETWORK ARCHITECTURE

Table 8: Neural network architecture for the one dimensional chaotic systems. d is the state dimension and L is the latent feature dimension.

Components	Layer	Weight size	Bias size	Activation
Encoder	Fully Connected	$m \times 10m$	$10m$	ReLU
Encoder	Fully Connected	$10m \times 10m$	$10m$	ReLU
Encoder	Fully Connected	$10m \times L$	L	
Forward operator $\hat{\mathcal{G}}_c$	Fully Connected	$L \times L$	0	
Forward operator $\hat{\mathcal{G}}_m$	Fully Connected	$L \times L$	0	
Backward operator $\hat{\mathcal{G}}_m^*$	Fully Connected	$L \times L$	0	
Decoder	Fully Connected	$L \times 10m$	$10m$	ReLU
Decoder	Fully Connected	$10m \times 10m$	$10m$	ReLU
Decoder	Fully Connected	$10m \times m$	m	

Table 9: Model architecture for Kolmogorov Flow

Components	Layer type	Layer number	Channels, (H, W)	Activation
Patch embedding	Convolution2d	1	$1 \rightarrow 32, (64, 64)$	
Encoder	Transformer Block	2	$32 \rightarrow 64, (32, 32)$	ReLU
Encoder	Transformer Block	3	$64 \rightarrow 128, (8, 8)$	ReLU
Encoder	Transformer Block	3	$128 \rightarrow 128, (2, 2)$	ReLU
Contraction operator $\hat{\mathcal{G}}_c$	Fully Connected	1	$128 \times 2 \times 2, -$	
Measure-invariant operator $\hat{\mathcal{G}}_m$	Fully Connected	1	$128 \times 2 \times 2, -$	
Backward operator $\hat{\mathcal{G}}_m^*$	Fully Connected	1	$128 \times 2 \times 2, -$	
Decoder	Transformer Block	3	$128 \rightarrow 128, (8, 8)$	ReLU
Decoder	Transformer Block	3	$128 \rightarrow 64, (32, 32)$	ReLU
Decoder	Transformer Block	2	$64 \rightarrow 32, (64, 64)$	ReLU
Decoder	Convolution2d	1	$32 \rightarrow 1, (64, 64)$	

G.2 DATASET.

(1) Lorenz 63: A 3-dimensional simplified model of atmospheric convection, known for its chaotic behavior and sensitivity to initial conditions. To learn our models, we generated a dataset consisting of 50 trajectories of 80,000 timesteps from random conditions. (2) Lorenz 96: A surrogate model for atmospheric circulation, characterized by a chain of coupled differential equations. We generated three datasets corresponding to 9, 40, and 80-dimensional states, respectively, each consisting of 2,000 trajectories with 1,500 timesteps. (3) Kuramoto-Sivashinsky equation: A fourth-order nonlinear partial differential equation that models diffusive instabilities and chaotic behavior in systems, such as fluid dynamics, and reaction-diffusion processes. We sampled a 128-dimensional dataset consisting of 1,000 trajectories with 500 timesteps from the dataset¹⁰. The description of the three dynamical systems is listed in Appendix F).

¹⁰Dataset for Kuramoto-Sivashinsky: <https://zenodo.org/records/7495555>

G.3 TRAINING DETAILS AND BASELINES.

At a high level, PFNN and other baselines are implemented in **Pytorch** (Paszke et al., 2019). Both the training and evaluations are conducted on multiple A100s and Mac Studio with a 24-core Apple M2 Ultra CPU and 64-core Metal737 Performance Shaders (MPS) GPU. The evaluation is conducted on the CPU.

- **LSTM:** The implementation is based on the provided code of <https://github.com/pvlachas/RNN-RC-Chaos>.
- **Koopman operator:** The implementation is based on the provided code of <https://github.com/dynamicslab/pykoopman>.
- **FNO:** The implementation is based on the provided code of <https://pypi.org/project/fourier-neural-operator/>
- **MNO:** The implementation is based on the provided code of https://github.com/neuraloperator/markov_neural_operator.

H ABLATION STUDY

Refer to Table 10 next page.

Models	Short-term metrics (NRMSE(%) with standard deviation)			Long-term metrics (KL Divergence)				
	n = 100 steps (10s)	n = 500 steps (50s)	n = 1000 steps (100s)	PC1	PC2	PC3	PC4	PC5
$\gamma_1 = 0$	13.1755 \pm 1.5800	24.1675 \pm 0.7410	25.8691 \pm 0.4602	9.5887	11.804	12.4063	16.9723	14.3733
$\gamma_1 = 0.1$	12.0158 \pm 1.4086	23.2177 \pm 0.7471	24.8580 \pm 0.4292	7.7278	8.3548	8.2582	11.0016	11.9143
$\gamma_1 = 0.3$	11.9607 \pm 1.5545	22.0558 \pm 0.8203	23.7729 \pm 0.3989	9.2303	7.1571	5.9686	11.7539	6.9519
$\gamma_1 = 0.5$	12.2610 \pm 1.5682	23.2001 \pm 0.7418	24.8155 \pm 0.4448	9.2303	17.1571	7.9686	11.7539	7.0175
$\gamma_1 = 1$	15.8813 \pm 1.5676	24.2260 \pm 0.8564	25.8763 \pm 0.4796	54.5125	37.393	23.6634	23.2298	42.0535
$\gamma_2 = 0$	25.3307 \pm 1.6363	27.7657 \pm 1.0189	28.3367 \pm 0.7986	158.8283	110.6211	113.643	156.1905	144.0953
$\gamma_2 = 0.1$	25.3999 \pm 1.6352	28.3275 \pm 0.8731	28.9132 \pm 0.6475	89.1672	58.5734	100.247	67.9531	77.2474
$\gamma_2 = 0.3$	25.0902 \pm 1.6627	27.9227 \pm 0.9805	28.6240 \pm 0.7919	52.8225	171.7602	47.8601	195.7412	24.8655
$\gamma_2 = 0.5$	11.2610 \pm 1.5682	26.1509 \pm 0.7321	26.7405 \pm 0.4734	9.2303	7.1571	5.9686	11.7539	6.9519
$\gamma_2 = 1$	25.4087 \pm 1.5991	27.9922 \pm 1.0653	28.5408 \pm 0.7277	103.5022	42.0691	112.2703	99.2408	69.4257
$L = 128$	13.3220 \pm 1.2288	24.8996 \pm 0.7067	26.2252 \pm 0.5610	18.1267	89.2787	14.1537	13.7019	49.3100
$L = 256$	11.2610 \pm 1.5682	26.4232 \pm 0.6528	27.7517 \pm 0.4418	9.2303	7.1571	5.9686	11.7539	6.9519
$L = 512$	14.7879 \pm 0.7621	21.2001 \pm 0.7418	23.5999 \pm 0.4948	30.6129	15.5005	19.5719	45.6542	31.8792
$L = 1024$	21.4511 \pm 5.0988	66.3871 \pm 7.7594	78.3571 \pm 8.2562	283.6508	389.8976	620.1534	800.8029	439.4327
$L = 2048$	26.2002 \pm 6.2770	68.4793 \pm 9.6299	79.4856 \pm 9.5521	2055.672	2563.1742	2044.7927	2869.2644	2627.9830
$\frac{1}{c_{LSI}} = 1$	446.4194 \pm 1398.1260	-	-	7229.5386	7525.1045	7659.6764	8305.9996	8235.5889
$\frac{1}{c_{LSI}} = 3$	21.4311 \pm 5.3909	-	-	80.0486	19.3858	13.6621	19.977	10.4728
$\frac{1}{c_{LSI}} = 5$	11.2584 \pm 1.3119	22.8693 \pm 0.8401	24.0563 \pm 0.6238	9.2303	7.1571	5.9686	11.7539	6.9519
$\frac{1}{c_{LSI}} = 7$	10.9688 \pm 1.3619	23.3200 \pm 0.7374	24.1939 \pm 0.5691	10.2828	11.8646	5.6711	4.6851	7.3462
$\frac{1}{c_{LSI}} = 9$	10.9888 \pm 1.0712	23.7053 \pm 0.7025	24.8763 \pm 0.4796	9.5226	11.4618	8.1733	6.4484	7.1676

Table 10: Ablation experiments showing the effect of varying PFNN hyperparameters. Short-term metrics are measuring the NRMSE with standard deviation at steps 100, 500 and 1000. Long-term metrics measure the KL Divergence in 5 principle components between long-term predictions and test data. Unaltered hyperparameters are training epochs of 50, $\gamma_1 = 0.3$, $\gamma_2 = 0.6$, latent feature dimension $L = 512$ and log-Sobolev constant term $\frac{1}{c_{LSI}} = 5$.

2355
2356
2357
2358
2359
2360
2361
2362
2363
2364
2365
2366
2367
2368
2369
2370
2371
2372
2373
2374
2375
2376
2377
2378
2379
2380
2381
2382
2383
2384
2385
2386
2387
2388
2389
2390
2391
2392
2393
2394
2395
2396
2397
2398
2399
2400
2401
2402
2403
2404
2405
2406
2407
2408